

Resonance structures in kink-antikink collisions in a deformed sine-Gordon model

Patrick Dorey,^a Anastasia Gorina,^b Ilya Perapechka,^b Tomasz Romańczukiewicz^c and Yakov Shnir^d

^a*Department of Mathematical Sciences, Durham University, UK*

^b*Department of Theoretical Physics and Astrophysics, Belarusian State University, Minsk 220004, Belarus*

^c*Faculty of Physics, Astronomy and Applied Computer Science, Jagiellonian University, Kraków, Poland*

^d*BLTP, JINR, Dubna 141980, Moscow Region, Russia*

E-mail: p.e.dorey@durham.ac.uk, nastya.gorina.2931@gmail.com,
jonahex111@outlook.com, tomasz.romanczukiewicz@uj.edu.pl,
shnir@theor.jinr.ru

ABSTRACT: We study kink-antikink collisions in a model which interpolates smoothly between the completely integrable sine-Gordon theory, the ϕ^4 model, and a ϕ^6 -like model with three degenerate vacua. We find a rich variety of behaviours, including integrability breaking, resonance windows with increasingly irregular patterns, and new types of windows near the ϕ^6 -like regime. False vacua, extra kink modes and kink fragmentation play important roles in the explanations of these phenomena. Our numerical studies are backed up by detailed analytical considerations.

KEYWORDS: soliton collisions, resonant structure, fractal

ARXIV EPRINT: [XXXX.XXXX](#)

Contents

1	Introduction	1
2	The Model	3
2.1	Model structure	3
2.2	Spectral structure	6
2.3	The double kink	8
2.4	Small perturbations of the double kink	9
2.5	Further static solutions: the unstable lump	10
3	Numerical methods and overall results	12
4	The first transition: from sine-Gordon to ϕ^4 scattering	13
4.1	False vacuum effects for small ϵ	13
4.2	Effective model	15
4.3	Perturbations from ϕ^4	17
5	The second transition: the emergence of the double kink	21
5.1	Multiple bound modes	21
5.2	Double kink collisions near the critical value of ϵ	26
5.3	Small kinks at critical ϵ	34
6	Conclusions	35

1 Introduction

The static and dynamic behaviour of kinks, that is topological solitons in 1+1 dimensional classical scalar field theories, has attracted much attention over the years; see e.g. [1–3]. In the classical sine-Gordon theory, the complete integrability of the field equations leads to constraints on the dynamics of these solitons via the infinite number of integrals of motion, as reviewed in [4]. As a result, the collision of sine-Gordon solitons cannot excite radiation modes, and the asymptotic structure of the final configuration only differs from what would have been found in the absence of any interaction by a set of phase shifts.

However, integrable models are exceptional, and most physical theories do not belong to this class. Usually, an integrable model can be considered as an approximation to a more realistic theory, and while some features of the integrable model may still persist in a deformed non-integrable system, others are lost, often in interesting ways. Aspects of this

interplay between integrable and quasi-integrable models have attracted a lot of attention recently, see e.g. [5–7]. One example is the modified sine-Gordon model of [8, 9] which still supports kink solutions, though their scattering is much more complicated than in the original integrable model. The presence of defects (or impurities) and boundaries can also destroy the complete integrability of the sine-Gordon theory in a variety of ways [10–12].

The ϕ^4 theory is similar to the sine-Gordon model in that they both support topological kinks, but the ϕ^4 theory is not exactly integrable, and there is radiative energy loss in kink-antikink ($K\bar{K}$) collisions. Associated with this is the resonant energy exchange mechanism and the resulting chaotic dynamics of kinks, see e.g. [13–18]. Numerical simulations of the ϕ^4 theory reveal that for certain initial velocities, the kink and antikink collide, become separated by a finite distance, then collide a second time before finally escaping to infinity. This is known as a (two-bounce) resonance window [13, 14]. Solitons can also escape after three or more consecutive collisions, leading to an intricate nested structure of multi-bounce windows [13, 14]. These resonance windows are related to the reversible exchange of energy between the translational mode of the ϕ^4 kink and its internal mode [13, 14]. This mechanism can be reasonably well approximated in a truncated model, which takes into account only two dynamical degrees of freedom, the collective coordinates of the kink and the internal mode [13, 15, 19, 20]. This approach is qualitatively effective but many attempts to derive it from first principles have been plagued by many ambiguities and discrepancies, see [20–22], although recent developments [23, 24] show some promising results. Furthermore, some modifications of the ϕ^4 model, see e.g. [25–27], allow for existence of towers of internal modes localized on the kinks. Clearly, in such cases a simple resonance energy exchange mechanism cannot be applied.

Resonance structures can also be observed in the triply-degenerate ϕ^6 model [18]. The kinks in this model do not support localized modes, and the resonance effects are instead determined by collective modes trapped by the $K\bar{K}$ system. A modification of the collective coordinate approach reproduces the resonance dynamics of the ϕ^6 $K\bar{K}$ collisions qualitatively well [19, 20].

The collective coordinate approximation is limited by the assumption that the modes which lead to resonances, and the modes of the continuum, are separated. However, as the frequency of the internal mode of a kink is shifted towards the mass threshold, an excitation of this mode may also excite the radiative modes of the continuous spectrum, affecting the resonance exchange mechanism. This motivates the current paper, an investigation of in $K\bar{K}$ collisions in a deformation of the sine-Gordon theory, other aspects of which were recently studied in [28]. The deformation lifts the infinite degeneracy of the sine-Gordon vacuum while leaving a \mathbb{Z}_2 symmetry unbroken. For small values of the deformation parameter, close to sine-Gordon, the model possesses two true vacua and a large number of false vacua. These open new channels of $K\bar{K}$ collisions via the excitation of a bubble of false vacuum and its subsequent decay, allowing a smooth transition from the kink-

antikink reflection that occurs in the deformed theory to the kink-antikink transmission found in sine-Gordon. At larger values a rich variety of behaviours is found: first, a simple deformation of the ϕ^4 pattern of resonance windows but then, as the kinks of the model acquire more localised modes, a much less regular pattern of windows together with transient structures we call pseudowindows. Finally, close to the critical coupling at which the model has three degenerate vacua, the kinks and antikinks partially fragment into subkinks and their scattering decomposes into a series of pairwise interactions, leading to a novel pattern of windows akin to recent studies of the scattering of wobbling kinks in the ϕ^4 theory [29].

The paper is organised as follows. In Section 2 we review the deformed sine-Gordon model of [28]. We also discuss the dependence of the spectral structure of linear perturbations of the solutions on the value of the deformation parameter, and the fragmentation of kinks and antikinks which occurs as the ϕ^6 -like limit is approached. Section 3 explains the numerical methods we used to investigate kink scattering in this model, and gives a birds-eye view of our results. In Section 4 we present our detailed results for kink-antikink collisions in the first regime of interest, where the model transitions from sine-Gordon to ϕ^4 behaviour, and discuss the resonance structures we observed. The collisions of kinks in the second regime, where the ϕ^4 model moves to a ϕ^6 -like model, are discussed in Section 5. Conclusions and further remarks are contained in the last section.

2 The Model

2.1 Model structure

We consider the simple theory of real scalar field in 1+1 space-time dimensions specified by the Lagrangian

$$L = \frac{1}{2} \partial^\mu \phi \partial_\mu \phi - U(\phi) \quad (2.1)$$

where the self-interaction potential $U(\phi)$ is

$$U(\phi) = (1 - \epsilon) (1 - \cos \phi) + \frac{\epsilon \phi^2}{8\pi^2} (\phi - 2\pi)^2, \quad (2.2)$$

and ϵ is a real positive parameter.

This model was proposed in [28] to investigate the decay of large amplitude breather-like states; our goal here is rather to study the collisional dynamics of its solitons, which turns out to be surprisingly rich. The parameter ϵ controls the deformation away from the infinitely-degenerate periodic sine-Gordon potential, which is recovered in the limit $\epsilon = 0$, as shown in figure 1. For any non-zero value of ϵ , the infinite dihedral group symmetry of the initial potential is broken down to \mathbb{Z}_2 , generated by a reflection around $\phi = \pi$. For $\epsilon < 0$ the energy is not bounded from below, and we therefore exclude these values. In addition, for $\epsilon > \epsilon_{cr}$, where

$$\epsilon_{cr} = \frac{16}{16 - \pi^2} \approx 2.609945762, \quad (2.3)$$

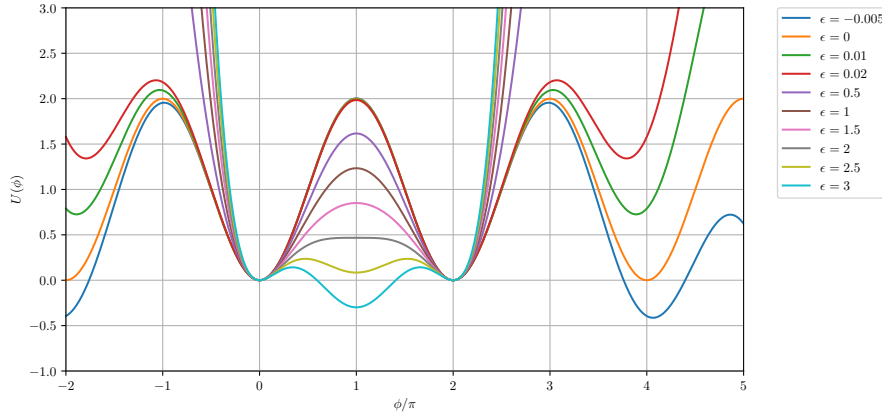


Figure 1. The potential of the model (2.1) for various values of the parameter ϵ . Note that the first and last values plotted are outside the range considered in this paper: for $\epsilon = -0.005$ the potential is unbounded below, while for $\epsilon = 3$ it does not support finite-energy kink solutions.

the potential has a single global minimum at $\phi = \pi$ and the model does not support static kink solutions, so we exclude these values too, and confine our attention to the range $0 \leq \epsilon \leq \epsilon_{cr}$. For all ϵ in the interior of this range, the potential has just two global minima, at $\phi = 0$ and $\phi = 2\pi$, and the model is parametrised in such a way that small perturbations around these true vacua always have mass equal to 1. In addition to these perturbative states, the model has kink and antikink solutions which interpolate between the global minima, the kinks interpolating between $\phi = 0$ at $x = -\infty$ and $\phi = 2\pi$ at $x = +\infty$ and the antikinks doing the opposite. (We will often be a little loose in our language and refer to topological lumps of either kind as kinks.) Some examples are shown in figure 2, and our aim in the following is to analyse how they scatter.

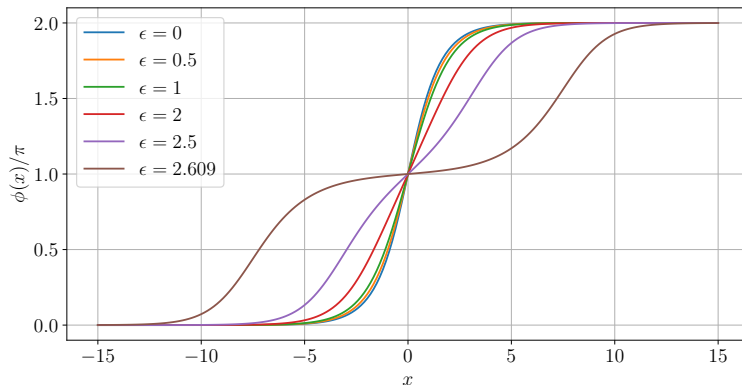


Figure 2. Examples of static kink solutions of the model (2.1) for various values of the parameter ϵ .

In addition to the true vacua, the model's potential has a number of the local minima corresponding to false vacua, which can influence kink scattering in important ways. It is

possible to consider perturbations around these false vacua, as long as they remain small. In such cases, for any local minimum ψ of the potential with $U'(\psi) = 0$, the square of the mass of small perturbation is $U''(\psi)$. The false vacua vanish when this mass tends to zero. These critical points are therefore defined by the pair of nonlinear equations (for ϕ and the parameter ϵ)

$$\frac{\partial U}{\partial \phi} = 0, \quad \frac{\partial^2 U}{\partial \phi^2} = 0. \quad (2.4)$$

These critical points allow us to determine the vacuum structure of the model. For example for $0.00105685 < \epsilon < 0.0074737$ there are four false vacua, near $\phi \approx -4\pi, -2\pi, 4\pi, 6\pi$, while for $0.0074737 < \epsilon < 0.0507066$ there are two false vacua (near $\phi \approx -2\pi$ and 4π), and for $0.0507066 < \epsilon < 2$ there are only the two true vacua ($\phi = 0$ and $\phi = 2\pi$).

Setting $\epsilon = 1$ yields a shifted and rescaled potential of the ϕ^4 model. Increasing ϵ further decreases the height of the potential barrier between the two vacua, and for $\epsilon > 2$ the local maximum at $\phi = \pi$ splits into two humps located in the intervals $\pi < \phi < 2\pi$ and $0 < \phi < \pi$, with a local minimum between them at $\phi = \pi$. For $2 < \epsilon < \epsilon_{cr}$ this minimum corresponds to a false vacuum, and for ϵ in this range the potential (2.2) has a very similar shape to that of the ϕ^6 model considered many years ago by Christ and Lee [25]. The mass of small fluctuations about this false vacuum is

$$m_1(\epsilon) = \sqrt{U''(\pi)} = \sqrt{(\epsilon - 2)/2}. \quad (2.5)$$

Finally, at $\epsilon = \epsilon_{cr}$ the vacuum at $\phi = \pi$ becomes degenerate with those at $\phi = 0$ and 2π , and the model resembles the triply-degenerate ϕ^6 model that was found to exhibit resonant scattering in [18].

The field equation of the model (2.1) can be written as

$$\phi_{tt} - \phi_{xx} + (1 - \epsilon) \sin \phi + \frac{\epsilon \phi}{2\pi^2} (\phi - \pi) (\phi - 2\pi) = 0. \quad (2.6)$$

For all $\epsilon \in [0, \epsilon_{cr})$, the static kink $\phi_K(x; \epsilon)$ depends parametrically on ϵ and interpolates between the vacua $\phi = 0$ as $x \rightarrow -\infty$ and $\phi = 2\pi$ as $x \rightarrow \infty$. In two cases its form is known analytically:

$$\phi_K(x; \epsilon = 0) = 4 \arctan e^{x-x_0}; \quad \phi_K(x; \epsilon = 1) = \pi \left(\tanh \frac{x-x_0}{2} + 1 \right). \quad (2.7)$$

There is little visual difference between these two solutions, as can be seen from figure 2. Despite their similarity, the dynamical properties of these kinks are very distinct, as will be seen below. Stronger deformations of the potential (2.2) significantly affect not just the scattering but also the form of the topological solitons, and as the deformation parameter approaches the critical value ϵ_{cr} , they become almost decomposed into pairs of subkinks interpolating between the true vacua at $\phi = 0$ and 2π via the false vacuum at $\phi = \pi$, as

also shown in figure 2. In the limit $\epsilon \rightarrow \epsilon_{cr}$ the potential becomes triply degenerate and the kinks split into two, in the corresponding different topological sectors.

The mass of the kink,

$$M(\epsilon) = \int_0^{2\pi} \sqrt{2U(\phi)} d\phi, \quad (2.8)$$

can be obtained from the standard Bogomolnyi' trick. It decreases from $M(0) = 8$ through $M(1) = \frac{2\pi^2}{3} \approx 6.5797$ to $M(\epsilon_{cr}) \approx 2.6363$ (cf. figure 3). Note that this limiting mass as $\epsilon \rightarrow \epsilon_{cr}$ is exactly twice the mass of a 'true' single kink of the model at $\epsilon = \epsilon_{cr}$. The Bogomol'nyi trick also reduces the second order static field equation to the first order Bogomol'nyi–Prasad–Sommerfield (BPS) equation

$$\phi_x = \sqrt{2U(\phi)} \quad (2.9)$$

which is much easier to solve and requires only a single integration constant. The profiles assume the vacuum values at spatial infinities.

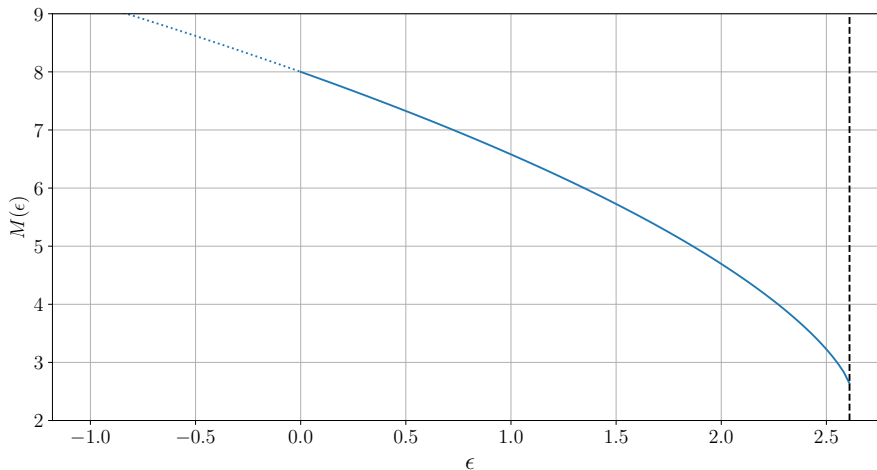


Figure 3. The mass $M(\epsilon)$ of a static kink as a function of the deformation parameter ϵ .

2.2 Spectral structure

We now consider the spectrum of linear perturbations of a single kink by setting $\phi(x, t) = \phi_K(x; \epsilon) + \eta(x, t)$ where $\eta(x, t) = \xi(x)e^{i\omega t}$. The corresponding equation for the fluctuation eigenfunctions is

$$\left(-\frac{d^2}{dx^2} + V(x) \right) \xi(x) = \omega^2 \xi(x) \quad (2.10)$$

where

$$V(x) = U''(\phi_K(x)) = (1 - \epsilon) \cos \phi_K(x) + \frac{\epsilon}{2\pi^2} (3(\phi_K(x) - \pi)^2 - \pi^2) \quad (2.11)$$

is the corresponding effective potential for the linear excitations, displayed in figure 4 for various representative values of ϵ . Note that the parameters of the model (2.1) are fixed

in such a way that the masses of the excitations around the true vacua $\phi = 0$ and $\phi = 2\pi$ remain the same and equal to 1, as in the original sine-Gordon model.

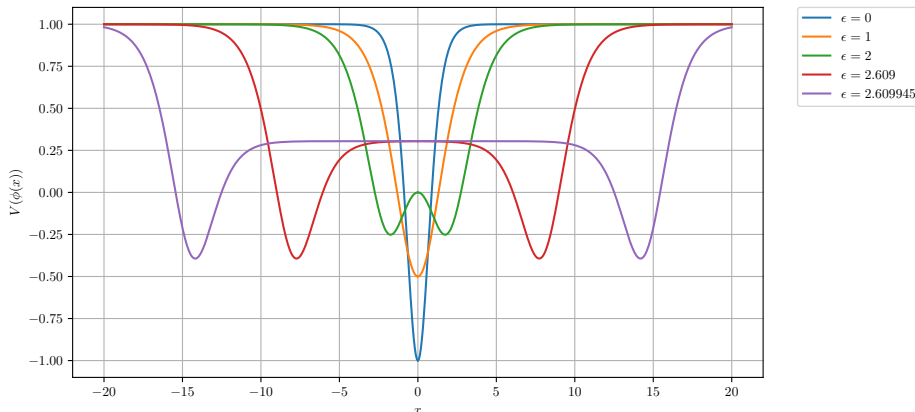


Figure 4. The linearized potential $V(x)$ (2.11) for various values of the deformation parameter ϵ .

We can solve (2.10) numerically for each value of the deformation parameter ϵ . For $\epsilon = 0$ the sine-Gordon model is undeformed, and the spectrum of linearized kink excitations does not contain any internal modes, but rather just the usual translational zero mode and the states of the continuum. These modes are not affected by the variation of the parameter ϵ , and exist for all of its values. However, as ϵ increases from zero an internal mode appears, its eigenfrequency ω_1 smoothly decreasing from the mass threshold with increasing ϵ as shown in figure 5, where we used the transformed parameter

$$\beta = \tanh^{-1}(\epsilon/\epsilon_{cr}) \quad (2.12)$$

for better visibility of the spectrum near the critical value $\epsilon = \epsilon_{cr}$.

For $\epsilon = 1$ the effective potential (2.11) reduces to the well-known Pöschl-Teller potential for the ϕ^4 theory. In this case the corresponding spectrum of fluctuations contains the translational zero mode $\omega_0 = 0$, one internal mode of the kink with frequency $\omega_1 = \sqrt{3}/2$, and the continuum modes $\omega_k = \sqrt{k^2 + 1}$.

For $\epsilon > 1$ more internal modes appear, their number tending to infinity as ϵ approaches ϵ_{cr} . Recall that for $2 < \epsilon < \epsilon_{cr}$ there is a false vacuum at $\phi = \pi$. As can be seen in figure 2 and as analysed in more detail in the next subsection, kinks in this region come to look like a pair of bound subkinks, the first interpolating $0 \rightarrow \pi$ and the second $\pi \rightarrow 2\pi$, rather than a single kink $0 \rightarrow 2\pi$. Each of these subkinks generates its own potential well, but these do not support localised modes. However the presence of the false vacuum yields an almost flat potential between the subkinks, as shown in figure 4. As $\epsilon \rightarrow \epsilon_{cr}$ the distance between the two subkinks tends to infinity. This limit corresponds to a very wide potential well, within which many bound modes can be trapped. At $\epsilon = \epsilon_{cr}$, the false vacuum $\phi = \pi$ becomes a true vacuum and the subkinks become independent topological defects. These

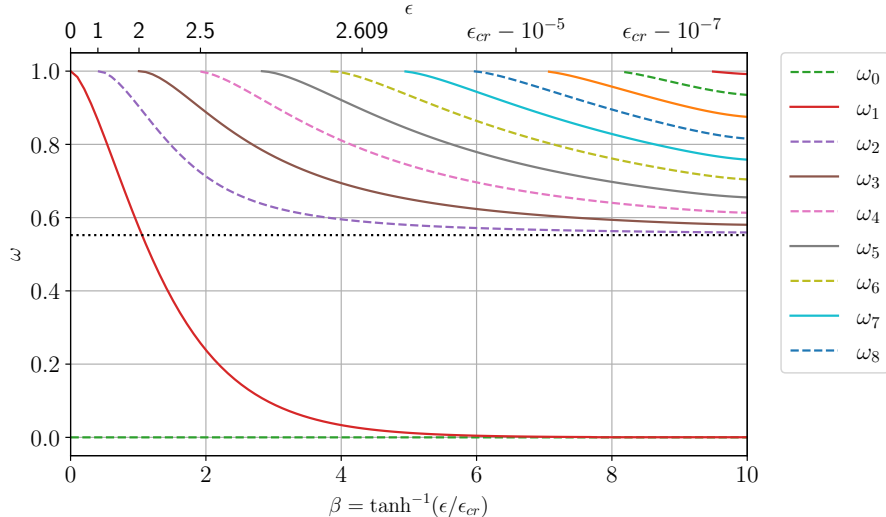


Figure 5. The eigenfrequency of the internal modes ω as a function of the deformation parameter $\epsilon = \epsilon_{cr} \tanh(\beta)$. Dashed lines correspond to even modes. The dotted line shows $m_1(\epsilon_{cr})$, the mass associated with small perturbations of the false vacuum at $\epsilon = \epsilon_{cr}$.

new, smaller kinks are not symmetric: they interpolate between one of the original two vacua $\phi = 0$ or $\phi = 2\pi$, for which the mass of the linearized perturbations is $m = 1$, and the new third vacuum at $\phi = \pi$. The mass of excitations about this vacuum is different, $m_1(\epsilon_{cr}) = \sqrt{\frac{\pi^2 - 8}{16 - \pi^2}} \approx 0.5522 < 1$. As can be seen by comparing figure 30 below with the corresponding plots in [18], the collisional dynamics of these new kinks is close to the resonant $K\bar{K}$ scattering observed in the ϕ^6 model, where the resonance structure appears not because of the presence of internal modes of the kinks but rather from collective modes trapped between them.

2.3 The double kink

A kink can fragment into subkinks when one (or more) false vacua lie between two true vacua. This occurs in our model as $\epsilon \rightarrow \epsilon_{cr}$, the single kink fragmenting into two subkinks separated by a region of false vacuum. The field of the subkinks situated at $x = \pm L$ approaches the false vacuum $\psi(\epsilon)$ as

$$\phi(x) - \psi(\epsilon) \approx \pm \frac{B}{m_1(\epsilon)} e^{\pm m_1(\epsilon)(x \mp L)}. \quad (2.13)$$

The constant B can be obtained from the numerical solution of the BPS equation (2.9). Its value depends on how we choose to define the positions of the subkinks. One natural choice is the point at which the field reaches the local maximum of potential. For $\epsilon = \epsilon_{cr}$ this is at $\phi = 1.367646$ and $\phi = 2\pi - 1.367646 = 4.915539$, for which $B = 1.210404$.

The force acting on the subkinks is a sum of the standard kink-kink repulsion (see for

example [1]) and the negative pressure of the false vacuum:

$$F = 2B^2 e^{-2m_1(\epsilon)L} - U(\psi(\epsilon)). \quad (2.14)$$

In this case $\psi(\epsilon) = \pi$ for all $\epsilon \in (2, \epsilon_{cr})$ and

$$U(\psi(\epsilon)) = \frac{16 - \pi^2}{8} (\epsilon_{cr} - \epsilon) \quad (2.15)$$

Static solutions balance between the scalar repulsion and false vacuum pressure, and the condition $F = 0$ gives the separation between the subkinks to be

$$L(\epsilon) = -\frac{1}{2m_1(\epsilon)} \log \left[\frac{U(\psi(\epsilon))}{2B^2} \right]. \quad (2.16)$$

Keeping only the lowest terms in $\epsilon_{cr} - \epsilon$ and using $m_1(\epsilon_{cr}) = \sqrt{\frac{\pi^2 - 8}{16 - \pi^2}}$ we obtain

$$L(\epsilon) = -\frac{1}{2} \sqrt{\frac{16 - \pi^2}{\pi^2 - 8}} \log \left[\frac{16 - \pi^2}{16B^2} (\epsilon_{cr} - \epsilon) \right] \quad (2.17)$$

or, in terms of β where near the critical value of ϵ we can use $\epsilon_{cr} - \epsilon \approx 2e^{-2\beta}$,

$$L(\beta) = \frac{1}{2} \sqrt{\frac{16 - \pi^2}{\pi^2 - 8}} \left[2\beta - \log \frac{16 - \pi^2}{8B^2} \right]. \quad (2.18)$$

This formula approximates the positions of the subkinks very well for large values of β .

2.4 Small perturbations of the double kink

The static solution representing a double kink balances the force repelling the subkinks and the attractive force due to the false vacuum trapped between them. When the subkinks are moved away from their equilibrium positions, say by some value δL , they will start to oscillate around these positions. Small displacements result in a returning force

$$\delta F = \frac{dF}{dL} \delta L = 2B^2 e^{-2m_1 L} (-2m_1) \delta L \quad (2.19)$$

but since at equilibrium $F = 0$ we can get rid of the constant B and write

$$\delta F = -2m_1 U(\psi) \delta L. \quad (2.20)$$

By taking into account that the mass of the subkink is a half of the mass of the full kink $M_{1/2} = M(\epsilon)/2$ we can find the frequency of the small oscillations:

$$\omega^2 = \frac{4m_1 U(\psi)}{M(\epsilon)}. \quad (2.21)$$

The leading term as $\epsilon \rightarrow \epsilon_{cr}$ is

$$\omega = \sqrt{\frac{(16 - \pi^2)(\epsilon_{cr} - \epsilon)}{2M(\epsilon_{cr})}} \approx 0.801 \sqrt{\epsilon_{cr} - \epsilon} \approx 1.83 e^{-\beta}. \quad (2.22)$$

These oscillations move the subkinks closer together and then further apart, corresponding to an antisymmetric excitation of the translational modes of the subkinks. This motion corresponds to the excitation of the first non-zero mode ω_1 of the full double kink, shown as a solid red curve on figure 5. We have checked numerically within the range $\epsilon_{cr} - \epsilon \in [10^{-5}, 10^{-2}]$, and $\omega_1(\epsilon)$ indeed scales as the square root of the difference $\epsilon_{cr} - \epsilon$ in this region, its numerical value agreeing with the approximation to at least three significant figures.

2.5 Further static solutions: the unstable lump

The presence of a false vacuum allows for another class of static solutions, albeit with infinite energy. These involve subkinks and subantikinks which interpolate between neighbouring true and false vacua. In scalar field theories a kink and an antikink always attract each other. However, if they are surrounded by a false vacuum with a true vacuum trapped in between, there is an additional force trying to separate them and thereby expand the region of true vacuum. For wide separations this force is constant, depending only on the difference between the field theoretic potentials in the false and true vacua. Since the attractive kink - antikink force decays exponentially, this opens a possibility that there is a single distance where the two forces balance. Note that perturbation in any direction would lead to growing acceleration, destroying the unstable static state.

In contrast to the situation for the double kinks, neighbouring true and false vacua are found both for ϵ small and for $\epsilon \rightarrow \epsilon_{cr}$. Suppose the relevant false vacuum is at $\phi = \psi$. In order to find the unstable solution we multiply the static version of (2.6) by ϕ_x and integrate once, imposing the false vacuum boundary condition $\phi = \psi$ at spatial infinity to find the BPS-like equation

$$\phi_x = \pm \sqrt{2[U(\phi) - U(\psi)]}. \quad (2.23)$$

The full-line solutions to this equation have zero topological charge and cannot be kinks: rather, they are unstable lumps, which can be viewed as static (sub-) kink and antikink pairs, as described in the opening paragraph of this section. The derivative ϕ_x vanishes before reaching the true potential minimum at one of the true vacua. Therefore we can apply the boundary condition at this point, thereby defining the position of the unstable solution:

$$U(\phi(0)) = U(\psi). \quad (2.24)$$

This is a transcendental equation for $\phi(0)$ and has to be solved numerically. But having the value $\phi(0)$ we can integrate the equation (2.23) with different signs for $x > 0$ and $x < 0$. Example solutions are shown in figure 6. Note that both for small (left panel) and near-critical (right panel) values of ϵ , the unstable solution develops an antikink-kink structure as the potential difference between the false and true vacua decreases.

For large separations (small values of ϵ or $\epsilon_{cr} - \epsilon$) we can use a similar approximation to that for the double kink and find the positions of the kink and antikinks with a few

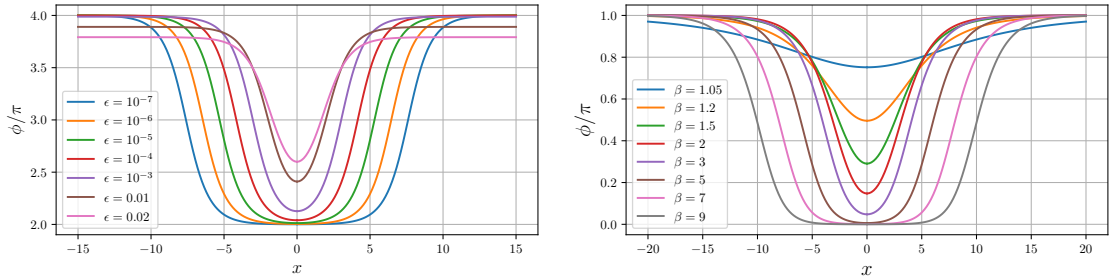


Figure 6. Profiles of unstable lumps. *Left:* unstable lumps for small values of ϵ based on the first false vacuum $\psi > 2\pi$; *right:* unstable lumps for $\epsilon \rightarrow \epsilon_{cr}$ based on the false vacuum at $\psi = \pi$ and parametrised by β , with $\epsilon = \epsilon_{cr} \tanh(\beta)$.

substitutions. The false vacuum is now on the outside pulling the kink and antikink apart and the true vacuum is trapped in between. Therefore in equation (2.16) m_1 has to be replaced by the mass of the true vacuum $m = 1$. For small values of ϵ the vacuum at $\phi = 4\pi$ is raised so that $U(4\pi) \approx 4\pi^2\epsilon$. Since the profiles of the kinks are known in the unperturbed model we can calculate $B = 4$ explicitly. This leads to

$$L(\epsilon) = -\frac{1}{2} \log \left(\frac{\pi^2 \epsilon}{4} \right) \quad (2.25)$$

which agrees well with the numerically found profiles. In the near critical case $U(\psi(\epsilon))$ is also known (2.15), but $B = 3.003373$ had to be determined numerically

$$L(\epsilon) = -\frac{1}{2} \log \left[\frac{16 - \pi^2}{16B^2} (\epsilon_{cr} - \epsilon) \right] = \frac{1}{2} \left[2\beta - \log \frac{16 - \pi^2}{8B^2} \right]. \quad (2.26)$$

In the case of unstable lumps the forces act in opposite directions than for double kinks, and equation (2.21) for the frequencies should therefore have the opposite sign (the true vacuum is inside and the false one outside), and instead of m_1 we can put 1 to yield

$$\omega^2 = -\frac{4U(\psi)}{M(\epsilon)}. \quad (2.27)$$

For $\epsilon \rightarrow 0$ we can use the mass of the sine-Gordon kink $M = 8$ and the limiting eigenfrequency of the unstable mode is therefore $\omega^2 = -4\pi^2\epsilon$. For $\epsilon \rightarrow \epsilon_{cr}$ we rather obtain

$$\omega^2 = -\frac{16 - \pi^2}{M(\epsilon_{cr})} (\epsilon_{cr} - \epsilon) \approx -2.325(\epsilon_{cr} - \epsilon) \approx -12.14 e^{-2\beta}. \quad (2.28)$$

On their own, these unstable lumps have infinite energy, because of the false vacuum surrounding them. However, as will be seen below, at least for $\epsilon \rightarrow \epsilon_{cr}$ they can still play an important role in the dynamics of the system when considered locally. Note that for $\epsilon \rightarrow 0$ there are further unstable lump solutions to the static field equations corresponding to a region of false vacuum embedded in a region of even more false (higher energy) vacuum.

These can be found and analysed exactly as above, but as we did not yet find a role for them in the scattering processes under consideration in this paper we will not discuss them further here.

3 Numerical methods and overall results

We used the method of lines to solve the second order evolution equation (2.6), discretizing the spatial part using the standard five point stencil on a uniform grid. Given the even parity of our initial conditions we solved on a half interval, implementing the appropriate boundary condition $\phi(-x) = \phi(x)$ at $x = 0$. For the second boundary condition we used the standard reflecting boundary, making sure to stop the evolution before any radiation could be reflected from the boundary and return to the centre of collision to interfere with the results. (Placing the second boundary at $x = T_s/1.8$, with T_s the total run-time of the simulation, was typically enough for this.) For the time stepping function we used a fourth order symplectic method which conserves energy and is reliable even for long time evolution for isolated hamiltonian systems. The spatial distance between the grid points was usually $dx = 0.05$ but we checked smaller values to verify the consistency of the results. The time step was usually set as $0.4dx$, but again, we also checked other values to confirm the convergence of our results.

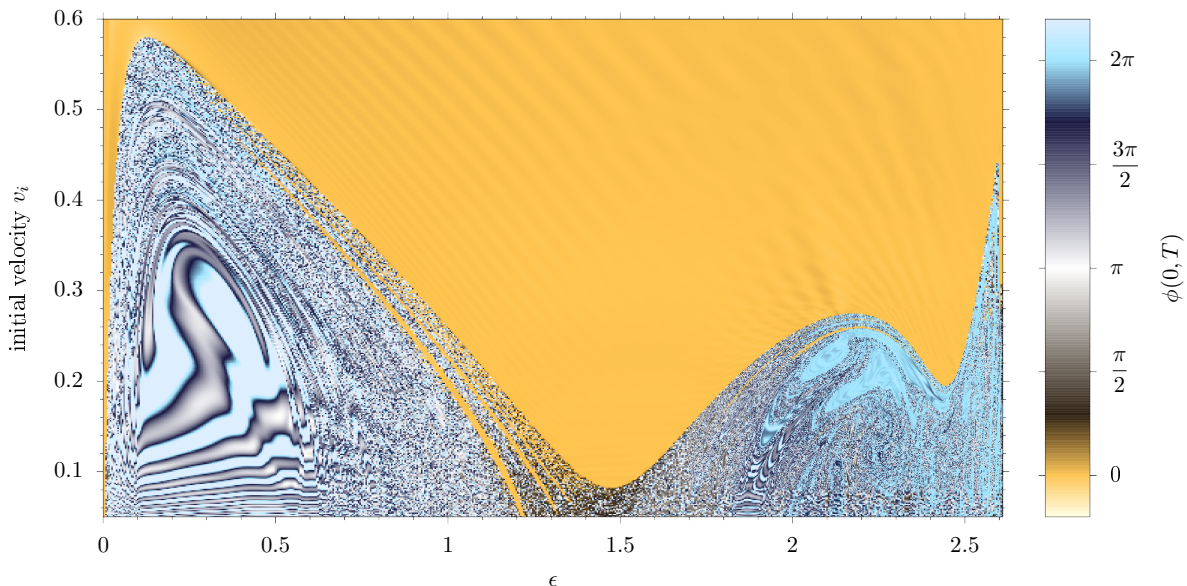


Figure 7. The post-collision value of the field at the collision centre as a function of the initial velocity of the colliding kinks and the deformation parameter ϵ . The field value was measured 300 units of time after the intersection of the initial trajectories, that is $300 + x_0/v_i$ units of time after the start of the simulation. Figures 20 and 21 below zoom in on the right-hand edge of this plot.

Figure 7 displays our results for $\bar{K}K$ collisions with initial conditions taken to be an antikink at $x = -x_0 = -20$ and a kink at $x = x_0 = 20$, with velocities v_i and $-v_i$

respectively, for the full range of values of $\epsilon \in [0, \epsilon_{cr}]$. The figure shows the post-collision value of the field at the centre of collision, as a function of v_i and the perturbation parameter ϵ . The field is measured 300 units of time after the moment of intersection of the initial antikink and kink trajectories, that is at $300 + x_0/v_i$ units of time from the start of the simulation.

Since the spectrum of linearized perturbations about a single kink depends strongly on the value of the deformation parameter ϵ , it is no surprise that the collisional dynamics of the kinks revealed in the figure has an intricate and varied structure. This structure is particularly rich near $\epsilon = \epsilon_{cr}$, and zoomed-in plots of this region are shown in figures 20 and 21 below. (For the last of these, figure 21, the increased widths of the antikink and kink in the regime plotted made it necessary to set $x_0 = 40$ to ensure that they were initially well separated.)

Figure 7 naturally splits into two parts: regime 1, $0 \leq \epsilon \lesssim 1.45$, which includes the interpolation between ϕ^4 and sine-Gordon like scattering, and regime 2, $1.45 \lesssim \epsilon \leq \epsilon_{cr}$, where the false vacuum at $\phi = \pi$ enters the picture and comes to play an important rôle as ϵ approaches ϵ_{cr} . In the following two sections we will analyse these regimes in turn.

4 The first transition: from sine-Gordon to ϕ^4 scattering

4.1 False vacuum effects for small ϵ

At $\epsilon = 0$ the model is integrable and scattering is perfectly elastic, and the vacua at 0 and 2π are exactly degenerate with further vacua at -2π , 4π and so on. An initial kink - antikink pair interpolating from 0 to 2π and then back to 0 scatters to an oppositely-ordered antikink - kink pair for which the intermediate vacuum is -2π . For any nonzero value of $\epsilon > 0$ such a final state is impossible, as value of the potential (2.2) at $\phi = -2\pi$ no longer degenerate with that at $\phi = 0$. Nevertheless, for small values of the parameter $\epsilon \lesssim 0.05$ the potential retains a false vacuum at $\phi \approx -2\pi$ (along with its \mathbb{Z}_2 reflection at $\phi \approx 4\pi$), as illustrated in figure 1. The presence of such false vacua significantly affects the dynamics of the kinks [30, 31]. In the model under consideration the collision channels associated with them enable a smooth transition from the situation for $\epsilon > 0$ back to sine-Gordon scattering at $\epsilon = 0$.

Figure 8 shows a collection of space-time maps of the scalar field through the collision process. As the impact velocity becomes large enough to overcome the potential barrier, a quasi-elastic sine-Gordon like scattering of the kinks with a flipping of the central vacuum from true to false is observed. In other words, the radiative losses are almost negligible, the collision of the solitons produces a bubble of false vacuum, with the outgoing kinks bounding the false vacuum domain within the true vacuum. For small values of ϵ the difference between the true and false vacuum energies is small and the dynamics of the

outgoing kinks can be treated using a thin wall approximation as in the problem of the decay of false vacuum, see [32–34].

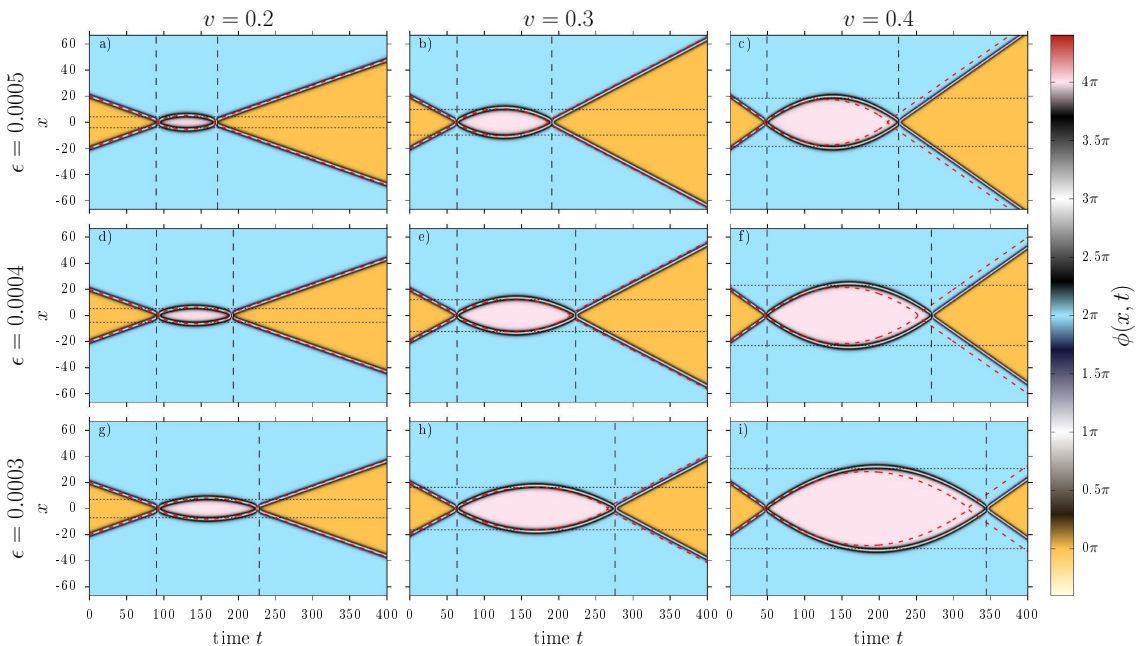


Figure 8. Collisions between an antikink and a kink with excitation of the false vacuum in the deformed model (2.1). The plots represent the field values as functions of the impact velocity and the time. Black dashed lines show the theoretically predicted bubble size and life-time. Red dashed lines show the paths calculated from the effective model (4.7). Note that the effective model is non-relativistic, and this is reflected in the worsening of its predictions with increasing velocities.

After the initial collision the new kinks bounding the false vacuum region move apart and decelerate [31, 35], stopping at the turning points $x = \pm L/2$ where the volume energy $16\pi^2\epsilon L$ of the bubble together with the bubble wall surface energy E_σ becomes equal to the initial kinetic energy of the colliding kinks, i.e.

$$E_\sigma + 16\pi^2\epsilon L = \frac{2M(\epsilon)}{\sqrt{1 - v_{in}^2}}. \quad (4.1)$$

Taking into account that in the thin wall approximation the mass of the kink is not very different from the mass of the sG kink $M = 8$, and $E_\sigma \approx 2M$, we find the maximal separation between the kinks bounding the false vacuum is

$$L = \frac{1}{\pi^2\epsilon} \left(\frac{1}{\sqrt{1 - v_{in}^2}} - 1 \right). \quad (4.2)$$

This is consistent with deceleration from the velocity v to 0 with a constant rate of $a_0 = \pi^2\epsilon$. From [35] and [1] we know that topological defects experience a force equal to the difference

between the field potential levels of the true and false vacua. In our case

$$F = U(4\pi) - U(2\pi) = U(0) - U(-2\pi) = 8\pi^2\epsilon = Ma_0. \quad (4.3)$$

The lifetime of the false vacuum bubble can also be calculated using the relativistic deceleration, giving

$$t_{bubble} = 2\sqrt{\frac{L}{a_0}(2 + a_0L)} = \frac{2v}{\pi^2\epsilon\sqrt{1-v^2}}. \quad (4.4)$$

The kinks then collide for a second time, and the resurrected $K\bar{K}$ pair finally separates in the true vacuum. The radiative energy loss for $\epsilon \ll 1$ is small, and thus the final escape velocity $v_{out} \approx v_{in}$. In the sine-Gordon limit $\epsilon \rightarrow 0$ the vacua become degenerate, t_{bubble} diverges, and the kinks collide perfectly elastically with a flip of the vacuum $2\pi \rightarrow -2\pi$ in the final state so that sine-Gordon scattering is restored.

4.2 Effective model

Figure 8 shows that as $\epsilon \rightarrow 0$ at fixed v the individual collisions become almost elastic, so we can neglect all radiation effects as well as the coupling to the bound mode. On the other hand, the false vacuum continues to be important: as just described, for all non-zero ϵ it leads to a recollision a time t_{bubble} after the initial collision, returning the vacuum at the origin to its original value of 2π , while for $\epsilon = 0$ there is no second collision, and the vacuum at the origin retains its flipped value of -2π in the final state. It is straightforward to construct and study an effective model in this limit of ϵ small but nonzero. For $\epsilon = 0$, analytic solutions describing $K\bar{K}$ collisions are known. For non-relativistic initial velocities we can adopt a moduli space approximation [23]

$$\phi(x, t) = 4 \arctan \left(\frac{\sinh a(t)}{\cosh x} \right). \quad (4.5)$$

For a and x large and positive, $\phi(x, t) \approx 4 \arctan(e^{a-x})$ and approximates a single antikink located at $x = a$; similar considerations in the other quadrants confirm that a is a modulus which asymptotically corresponds to the position of the antikink in the solution, with $-a$ being the position of the kink. In the sine-Gordon model, nonrelativistic scattering with velocity $v \ll 1$ is reproduced by setting $a(t) = a_{sg}(t)$ with

$$\sinh a_{sg}(t) = \frac{\sinh vt}{v}. \quad (4.6)$$

For small values of ϵ we can assume that the solution (4.5) approximates well the instantaneous shape of the field in the deformed model, replacing the above formula for $a_{sg}(t)$ with a general function $a(t)$. Putting this into the Lagrangian density and integrating over x we obtain a Lagrangian describing a single particle

$$L = \frac{1}{2}g(a)\dot{a}^2 - (1 - \epsilon)W_{sg} - \epsilon W_4 \quad (4.7)$$

where

$$g(a) = \int_{-\infty}^{\infty} \left(\frac{\partial \phi}{\partial a} \right)^2 dx = 16 \left(1 + \frac{2a}{\sinh(2a)} \right) \quad (4.8)$$

is a metric on the moduli space which plays the role of an effective mass, and

$$W_{sG,4} = \int_{-\infty}^{\infty} \left[\frac{1}{2} \left(\frac{\partial \phi}{\partial x} \right)^2 + U_{sG,4}(\phi) \right] dx \quad (4.9)$$

is an effective potential where $U_{sG}(\phi) = 1 - \cos \phi$ and $U_4(\phi) = \frac{1}{8\pi^2} \phi^2 (\phi - 2\pi)^2$ are the sine-Gordon and ϕ^4 parts of the self-interaction potential $U(\phi)$. The sine-Gordon integral can be calculated explicitly with the result

$$W_{sG} = 16 \left[1 - \frac{1}{2 \cosh^2(2a)} \left(1 + \frac{2a}{\sinh(2a)} \right) \right]. \quad (4.10)$$

Unfortunately we were unable to find a closed form of the effective potential coming from the ϕ^4 part, which we denote as W_4 . For large positive values of $a \gg 1$, corresponding to a kink - antikink pair, the effective potential tends to a constant, $W_4 \rightarrow 13.426$. Large negative values of $a \ll -1$ correspond to a ‘wrongly-ordered’ antikink-kink pair separated by a region of the false vacuum. In this case W_4 ultimately grows linearly with $|a|$, with gradient $16\pi^2$, since the false vacuum section of length $2|a|$ has the constant energy density of $\epsilon U(-2\pi) = -8\pi^2\epsilon$. Numerical integration for $a \ll -1$ gives an asymptotic form $W_4(a) \approx 157.91|a| - 188.52$, where the slope is equal to $16\pi^2$ as expected.

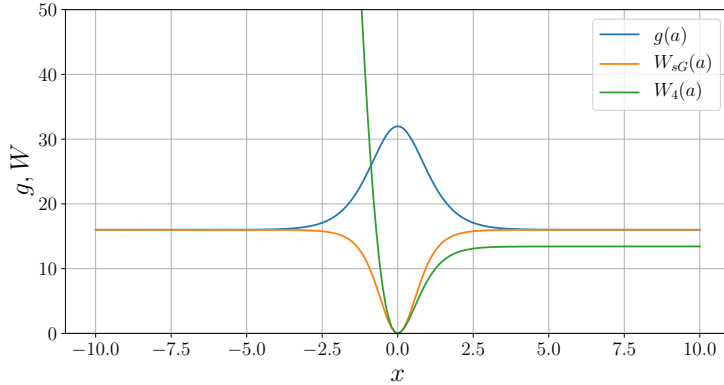


Figure 9. Metric and effective potentials for small values of ϵ

The three functions determining the effective dynamics are shown in figure 9, and trajectories obtained from this model are included as dashed red lines in figure 8. The discrepancy is greatest down the right hand column, as expected since the effective model should be most accurate for low velocities. Indeed, the effective model trajectories and those obtained from full simulations are identical within the resolution of the figure for $v = 0.2$. Figure 10 zooms in to the region of the first collision for the plots along the top

row of figure 8, showing that the effective model manages to capture the dynamics even when the kinks collide.

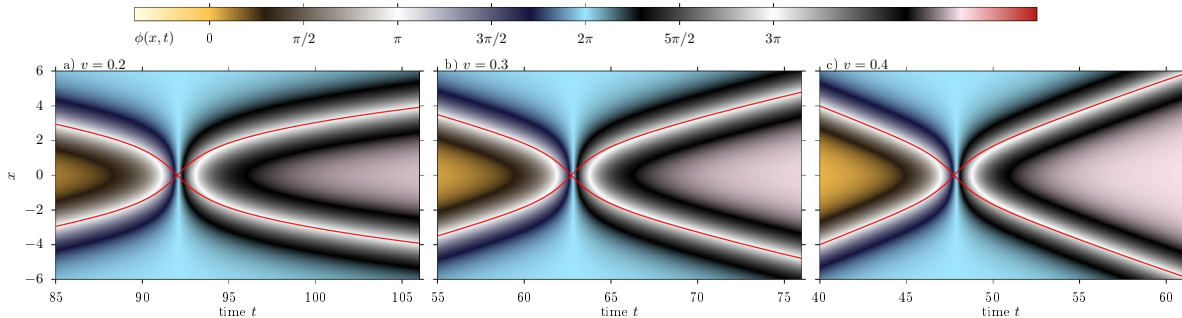


Figure 10. Close-up views of the initial collision for the top row of plots of figure 8, comparing the full field theory results with the predictions of the effective model, which are shown with continuous red lines.

4.3 Perturbations from ϕ^4

As ϵ increases beyond 0.05 the false vacuum at $\phi \approx -2\pi$ is lost, and after a transitional region the pattern of $\bar{K}K$ collisions comes to resemble the well-known resonant behaviour found in the ϕ^4 model [13–17], which is recovered for $\epsilon = 1$. Provided the initial velocity v_i of the colliding kinks is larger than an upper critical velocity v_c , they rebound and, while losing some of their velocity, escape back to infinity. Correspondingly the field at the origin reverts to its initial value of 0, coloured yellow on figure 7. For $v_i < v_c$, the rebounding kinks from the initial collision no longer have escape velocity and recollide at the centre, after which they generally form an oscillating bound state, a so-called bion (sometimes also called an oscillon in the literature¹), which slowly radiates the energy away, annihilating into the vacuum $\phi = 2\pi$ as $t \rightarrow \infty$. This vacuum is coloured blue on figure 7.

However it turns out that there are ‘windows’ of velocities well below v_c , within which the recolliding kinks recover their ability to escape. For initial velocities in these ranges, the kinks collide, separate to a finite distance and turn around to collide a second time, and then escape to infinity. In fact there is a tower of these ‘two-bounce’ windows of decreasing width, labelled by an integer ‘window number’ n related to the number of the oscillations of the kink’s internal mode between the two collisions [13–15]. This sequence of windows accumulates at the upper critical velocity v_c as $n \rightarrow \infty$.

These resonance windows are associated with the reversible exchange of energy between the internal and translational modes of the kinks, the condition for resonance leading to a prediction for the relationship between the window number n , the time interval between

¹Some authors make a distinction between the two terms, using the word oscillon for objects with well defined frequencies, but we will use the word bion for any form of slowly-decaying oscillating bound state throughout this paper.

the two collisions T , and the frequency ω_1 of the internal modes of the colliding kinks [14]

$$\omega_1 T = 2\pi n + \delta \quad (4.11)$$

where n counts the number of oscillations of the internal mode between the two collisions and δ is a phase shift which we fix, as in [14], to lie in the range $0 \leq \delta < 2\pi$. For some values of n the energy imparted to the kinks after the second collision, while still high, might not be enough to allow their escape. These correspond to so-called false windows.

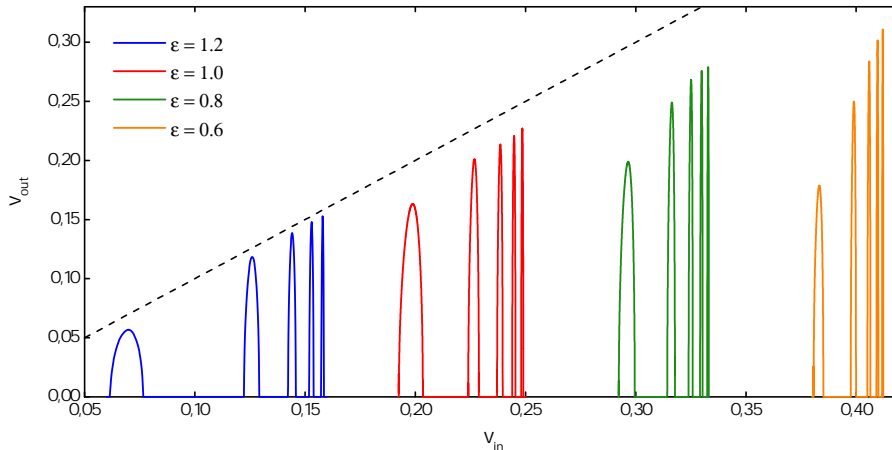


Figure 11. Two-bounce windows in regime 1: the final velocity of the kink-antikink pair as a function of the initial velocity for various values of the deformation parameter.

The picture of ϕ^4 -like resonant scattering just described is preserved in our model provided the deformation parameter ϵ is not too far from one. Figure 11 shows some typical patterns of two-bounce windows, plotting the final velocity of the kinks v_{out} as a function of the initial velocity v_{in} inside these windows for various values of ϵ , and showing that the deformed model (2.1) still supports sequences of resonance windows in this regime. Further three and higher bounce windows exist at the edges of each two-bounce window, but are not shown in the plot; we will not explore this aspect of the models in this paper.

Figure 12 plots the inter-collision times for these two-bounce windows against the window number n , showing that they satisfy the expected linear relationship (4.11), as for the ϕ^4 model. Fitted slopes and intercepts of the lines on the figure are given in table 1. The second and fifth columns show reasonable agreement, as predicted by (4.11).

We conclude that the pattern of these windows can be explained by the same give-and-take energy transfer mechanism as in the original ϕ^4 theory. The working of the resonance mechanism is clearly seen in figure 13, which shows field evolution at the origin inside the first four two-bounce windows for $\epsilon = 0.6$.

As the deformation parameter ϵ decreases from 1, the upper critical velocity v_c initially increases almost linearly, as can be seen in figures 7 and 11. At the same time the associated

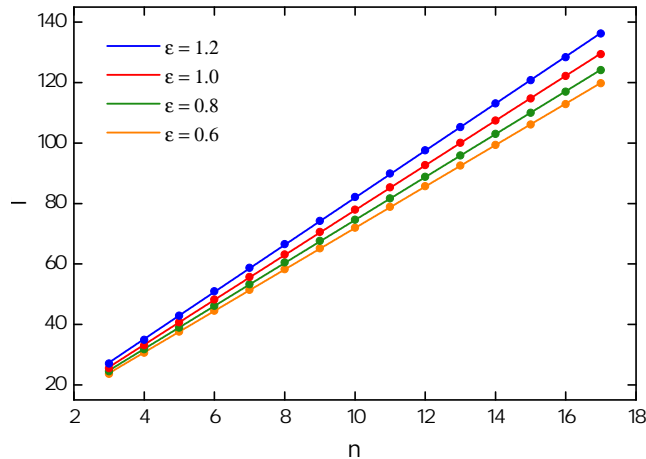


Figure 12. The time T between the two collisions as a function of the window number $n = 3 \dots 17$ for two-bounce resonance windows with $\epsilon = 1.2, 1, 0.8$ and 0.6 .

ϵ	slope	intercept	$\omega_1(\epsilon)$	$2\pi/\omega_1(\epsilon)$
1.2	7.7907	3.9929	0.82163761	7.647149146
1.0	7.4153	3.6165	0.86602540	7.255197456
0.8	7.1071	3.4486	0.90521781	6.941075670
0.6	6.8621	3.2652	0.93933673	6.688959440

Table 1. Linear fits for the lines on figure 12, with the slopes compared with the predictions of the resonance condition (4.11). The values of $\omega_1(\epsilon)$ follow from the (numerical except for $\epsilon = 1$) solution of the eigenvalue problem (2.10), as described in section 2.2.

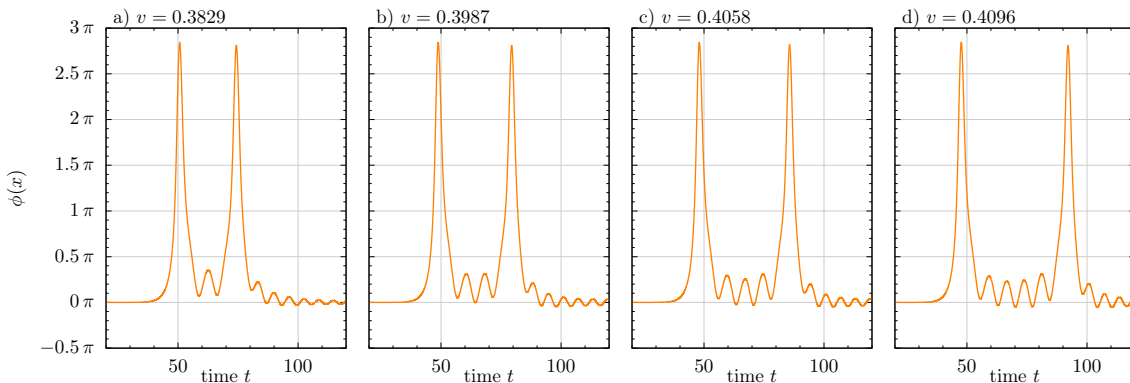


Figure 13. Field value at the collision centre as a function of time, showing the first four two-bounce resonance windows for $\epsilon = 0.6$. For this value of ϵ , $\omega_1 = 0.939337$ and $2\pi/\omega_1 = 6.68896$. These plots correspond to window numbers $n = 3, 4, 5$ and 6 in the formula (4.11).

windows, and the gaps between them, become narrower.

The maximal value of the upper critical velocity $v_c = 0.5803$ occurs for $\epsilon = 0.13$; the corresponding eigenvalue of the internal mode is $\omega \approx 0.975$. Evidently, as the frequency

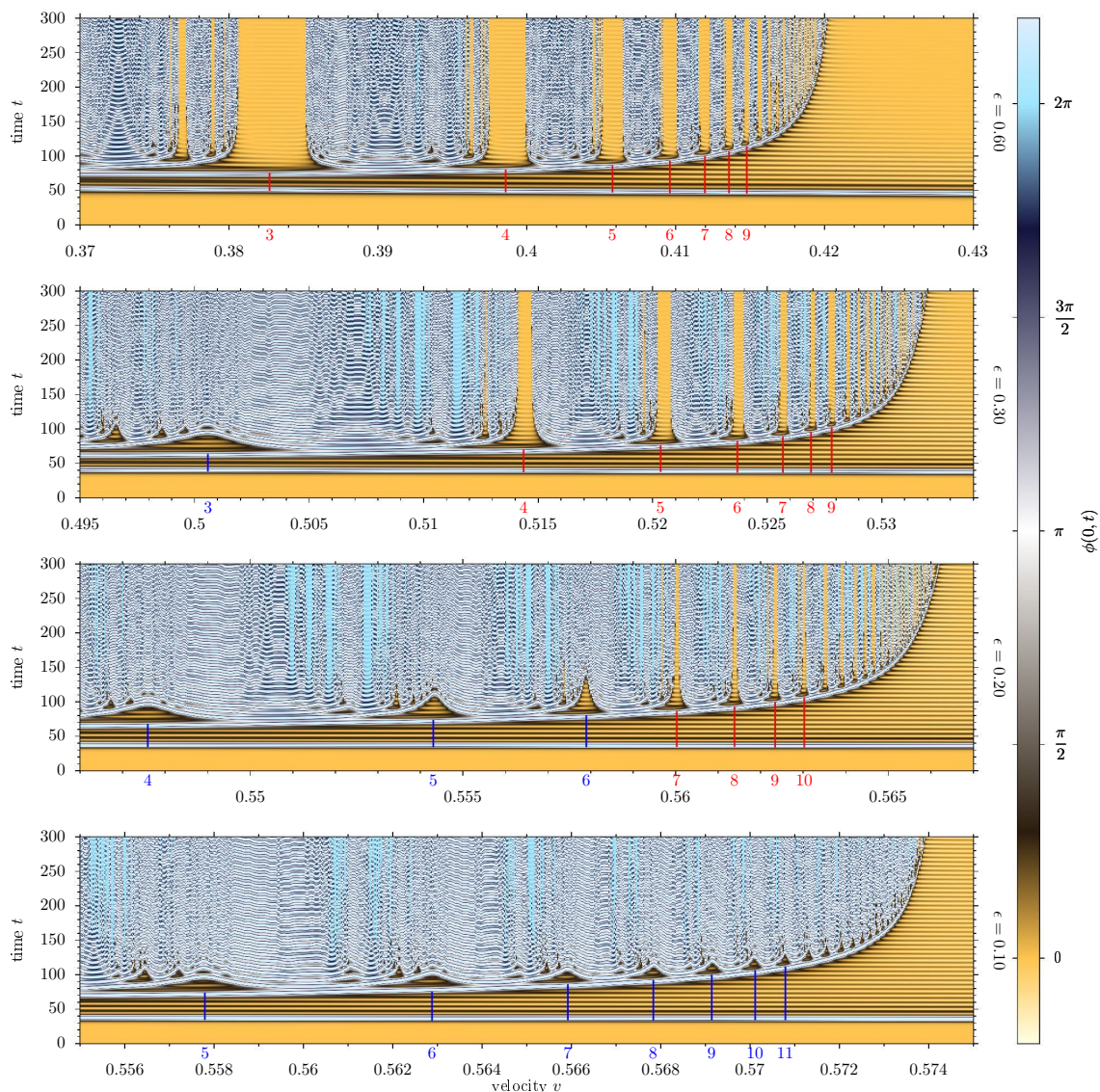


Figure 14. Kink-antikink resonance collisions in the model (2.1) for four values of the parameter ϵ in regime 1. The plots show the field value at the collision centre as a function of initial velocity v and time t from the start of the simulation. As ϵ decreases, the windows move to higher velocities, and some change from true windows to false windows. The window numbers are shown in red and blue below the plots; blue for false windows, and red for true ones.

of the internal mode is approaching the continuum threshold, an excitation of the internal mode may also affect the modes of continuum leading to energy loss due to radiation. This effect can destroy the fine mechanism of the reversible energy exchange in kink-antikink collisions. Indeed, we observe that the structure of resonance windows in $K\bar{K}$ collisions is damaged as ϵ decreases.

Surprisingly, the first two-bounce window that becomes false, at about $\epsilon = 0.35$, is the

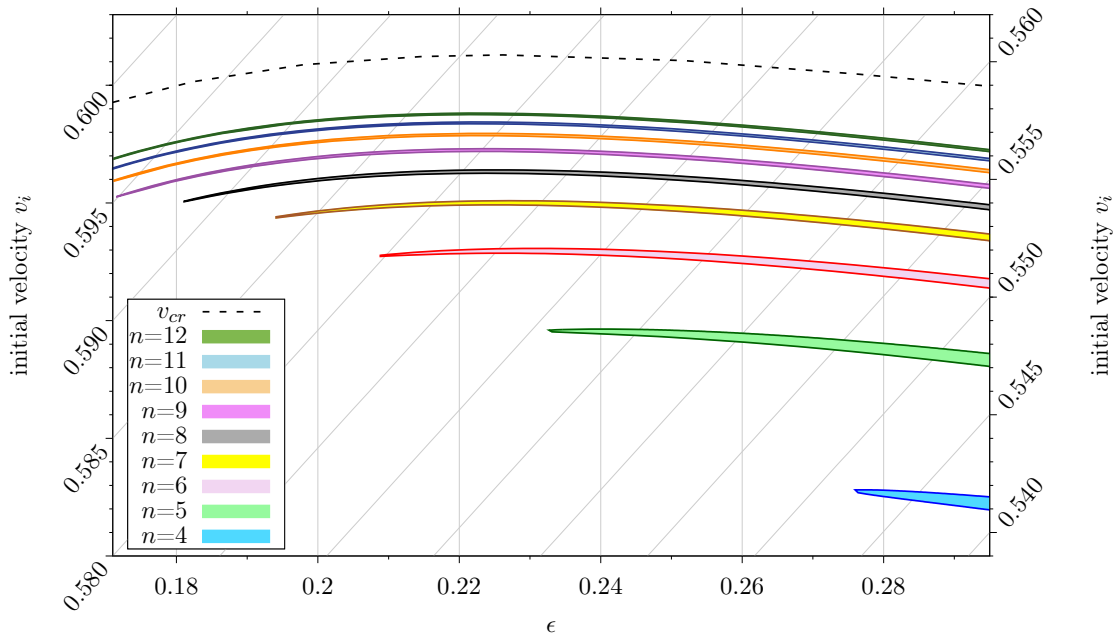


Figure 15. The closing two-bounce windows as a function of both ϵ and initial velocity v_i in a sheared coordinate system to reduce the high inclination of the structure.

one which was initially the widest, corresponding to the lowest number n of oscillations of the internal mode. Figure 14 shows the loss of true windows in action. In the top plot, with $\epsilon = 0.6$, all the windows seen at $\epsilon = 1$ are still open. As ϵ decreases through 0.35, the smallest-velocity window, for which $n = 3$, becomes false, as seen in the second plot, taken at $\epsilon = 0.3$. By the time ϵ has decreased to 0.2, shown in the third plot, three more windows have become false. Finally the bottom plot shows that all resonance windows have closed at $\epsilon = 0.1$. To show the pattern in more detail we located the two-bounce windows for $0.17 < \epsilon < 0.295$ and plotted them in figure 15. Because the upper critical velocity as well as the whole structure is a steep function of ϵ in this range ($\Delta v / \Delta \epsilon \approx 0.33064$) we used an affine transformation to reduce the shear effect and kept ϵ unchanged. The figure shows clearly that the windows with smaller values of n close first as ϵ decreases.

5 The second transition: the emergence of the double kink

5.1 Multiple bound modes

While the deformation parameter ϵ remains below 1, there is just one internal mode of the kink. As ϵ increases past this value, a second internal mode, with frequency ω_2 , emerges from the continuum, as shown in figure 5. The presence of this can be seen numerically in the power spectra of the field at the origin after a kink-antikink collision, shown in figure 16. The extra internal mode complicates the pattern of reversible energy exchange between the translational mode of the kinks and the internal modes, but while ϵ remains

below about 1.4, the frequency of the second mode ω_2 is not very far below the mass threshold, and the leading role in the resonance scattering mechanism still belongs to the lowest frequency internal mode ω_1 . The structure of ϕ^4 -like escape windows labelled by the oscillation number n of this mode survives, as seen in figure 17 (a) and the blue curves in figures 11 and 12. As ϵ increases through 1.25 these windows start to close, again starting from the smallest values of n , and by $\epsilon \approx 1.5$ they have all gone. The resonance condition is no longer given by the simple relation (4.11), and the interplay between the two internal modes becomes more important as ϵ increases further and the second mode becomes well separated from the continuum. The upper critical velocity v_c also begins to increase as ϵ becomes larger than 1.5, as seen in figure 7.

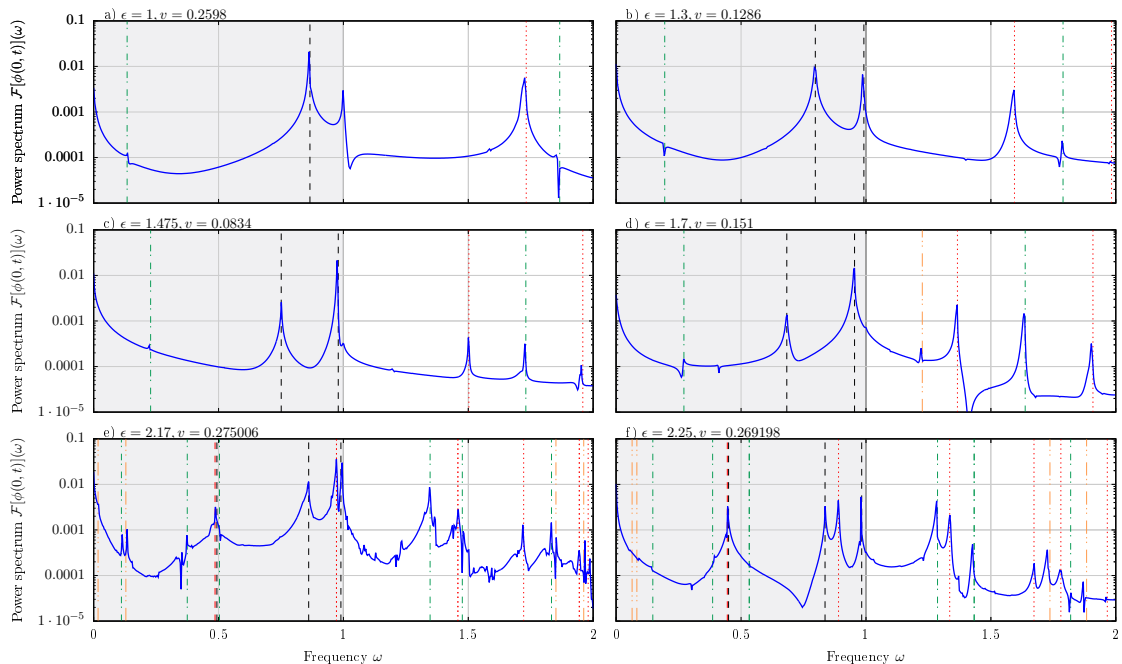


Figure 16. Power spectra of fluctuations at the origin after a kink-antikink collision for various values of ϵ from 1 to 2.25, showing signals of the extra internal kink modes which emerge as ϵ increases past 1 and then 2. The speeds of the incident kink and antikink, shown above each subplot, is chosen in each case to be just larger than v_c for that value of ϵ . Dashed black lines show the frequencies of the internal modes ω_1 , ω_2 and so on; red dotted lines are integer multiples of these frequencies; green dot-dashed lines are at $|\omega_i \pm \omega_j|$, $i \neq j = 1, 2, 3$; and orange dot-dashed lines at $|2\omega_1 \pm \omega_i|$, $i = 2, 3$.

Increasing ϵ further yields more complicated chaotic dynamics, and the sporadic reappearance of scattering windows below the upper critical velocity. The third internal mode appears in the spectrum of linearized perturbations while the frequencies of the first and the second modes continue to decrease. Figures 17 (b), (c) show the window structure

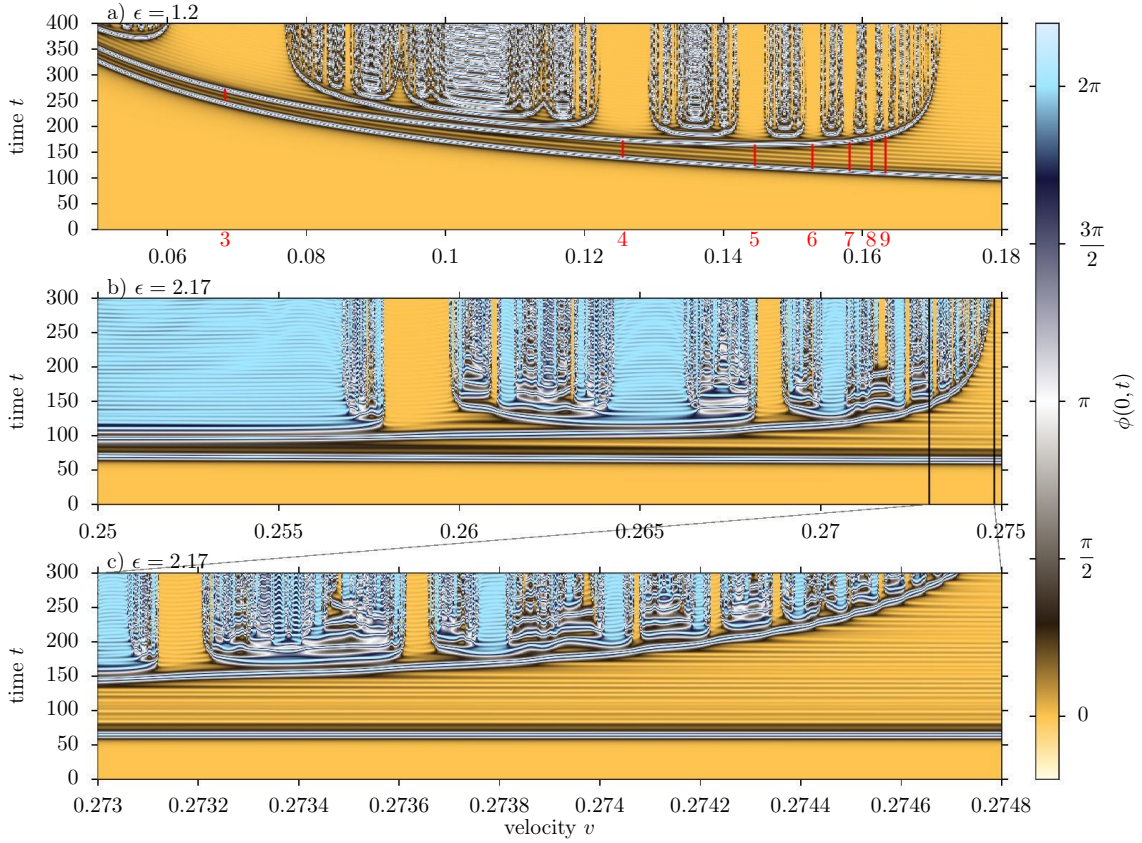


Figure 17. Field at the centre for $\epsilon = 1.2$ (a) and $\epsilon = 2.17$ (b), (c). Subplot (a) shows a regular structure of ϕ^4 -like windows labelled by the oscillation number n of the first internal mode, as seen for $\epsilon \leq 1$ in figure 14. Subplots (b) and (c) are taken for a value of ϵ for which the window structure is much more chaotic. The pattern includes a number of the blue ‘pseudowindows’ discussed more in the main text.

at $\epsilon = 2.17$, while figures 18 and 19 show some typical collision processes at the same value of ϵ . The windows again accumulate as the critical velocity v_c is approached, but the pattern is much less regular than the ϕ^4 -like resonant $\bar{K}K$ collisions considered thus far. The escape windows (indicated by the yellow colour) become less symmetric, as if one side of the window has merged with a false window. In addition, a set of light blue regions that we will call ‘pseudowindows’ appears. Their blue colour indicates that the centre field after collision is flipped into the $\phi = 2\pi$ vacuum. Topologically, this corresponds to an annihilation: the value of the field at the origin in the final state is equal to its value at infinity. However, instead of there being slowly-decaying bion at the centre (signalled by white-grey-black stripes on figure 17), as formed in a ϕ^4 -like $\bar{K}K$ capture, two bions are ejected in opposite directions, rapidly transporting most of the energy away from the origin and leaving the centre field oscillating around the 2π vacuum with a relatively small amplitude. The collisions shown in the second and third plots of figures 18 and 19 show

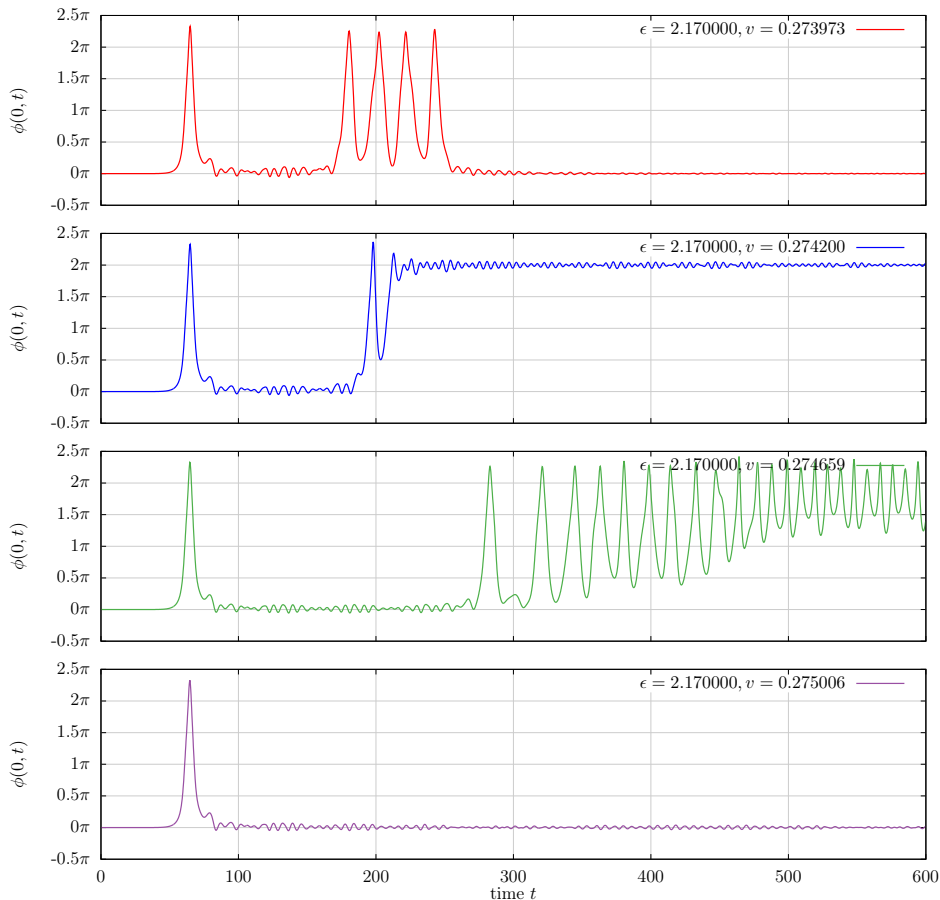


Figure 18. Evolution of the field at $x = 0$ for four values of the initial velocity with $\epsilon = 2.17$, $\beta = 1.19$ showing a true window, a pseudowindow, an annihilation to a centrally-located bion, and kink-antikink escape. The presence of higher modes can be seen in the more irregular oscillations of the field after the first collision compared to figure 13. Longer-time views of the full spacetime evolution of the field for these collisions are shown in figure 19 below.

this distinction clearly: both are examples of antikink-kink capture, but in the second plot a pair of bions is emitted and the central field relaxes quickly to 2π , while in the third plot a bion remains at the origin and the relaxation is much slower. Note that the concept of a pseudowindow relies on field measurements being taken at intermediate time scales, longer than the collision time but shorter than the time required for the radiative decay of a bion. At larger time scales the field at any fixed location, including the origin, will relax to one of the vacuum values, and so regions exhibiting white-grey-black stripes in our plots will ultimately revert to the same blue colour as the pseudowindows. Nevertheless, the extremely long lifetime of the bion means that the relevant time-scales are well separated, making the pseudowindows clearly visible. As discussed in the next section, more examples of this phenomenon can be observed for higher values of ϵ , closer to ϵ_{cr} . In fact, for very small values of ϵ some narrow pseudowindows also appear, as can be seen in figure 14.

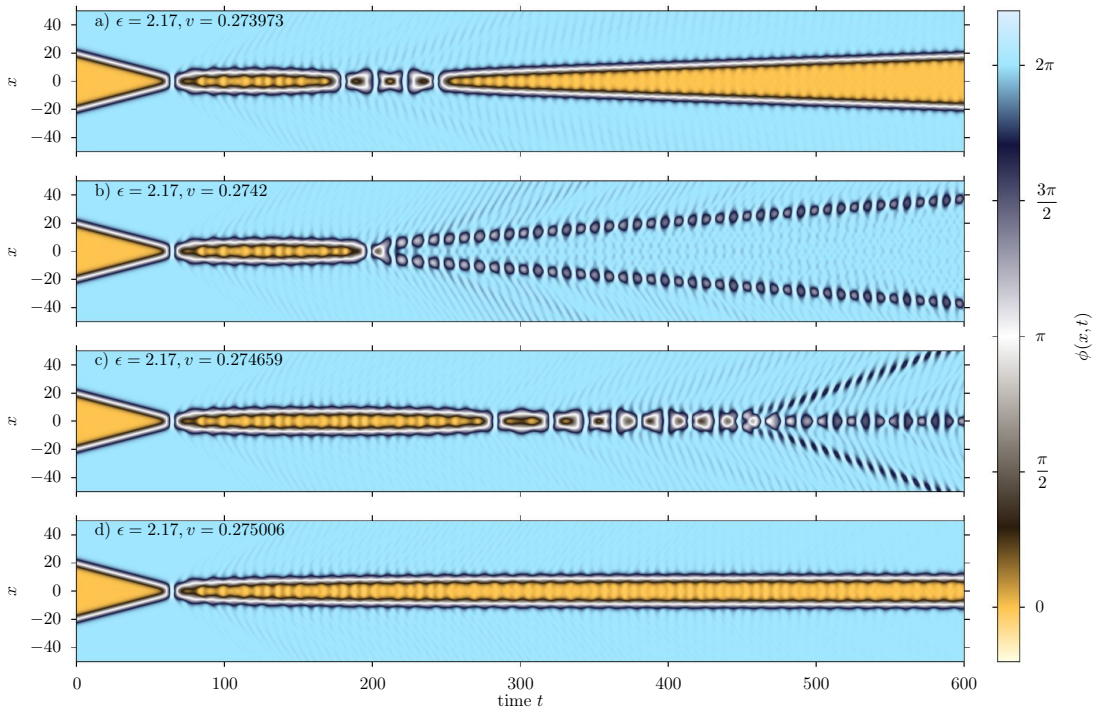


Figure 19. Spacetime plots of the four collisions of figure 18. The second plot shows the emission of a pair of bions at $t \approx 200$, which rapidly transport energy away from the central region. The centrally-located bion in the third plot emits a burst of radiation at $t \approx 460$; this is an example of the stacatto radiation phenomenon discovered in [28].

The full scan shown in figure 7 and the closer zoom for ϵ near to ϵ_{cr} plotted in figure 20 show that the critical velocity oscillates as ϵ increases beyond 1.5. A possible explanation for this effect is that the local maxima of the escape velocity correspond to maximal loss of the energy due to radiation. This can happen when two conditions are fulfilled: (i) a large amount of energy is transferred to one of the internal modes; (ii) this mode quickly radiates the energy away via the coupling to the continuum. Indeed, the modes closest to the mass threshold radiate the most. One of the modes is also exactly at the threshold for $\epsilon = 0$. However, this value corresponds to the integrable sine-Gordon model. Hence, the threshold mode is decoupled from the solitonic degrees of freedom, and cannot be excited during collisions. As a matter of fact, the first local maximum of the critical velocity is for $\epsilon = 0.131$ for which the internal mode reaches $\omega = 0.9951$. Similar values of frequencies of odd modes are reached for two more local maxima (Table 2).

Another intriguing observation is that the local minima of the critical velocity correspond to the values of ϵ for which one of the frequencies reaches the value $3/4$ (within 1% error). This might indicate that some $3 : 4$ resonance with the threshold frequency plays an important role in the collision process. Note that this resonance can happen for both even and odd modes, whereas the maxima are only for the odd modes. This may mean

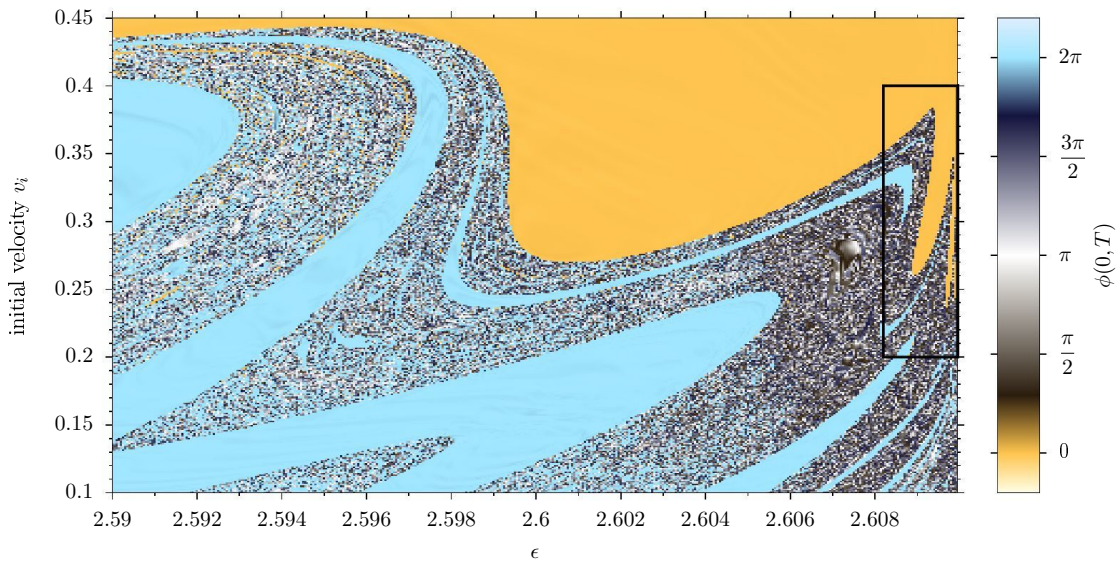


Figure 20. The post-collision value of the field at the collision centre as a function of initial velocity of the colliding kinks, and the deformation parameter ϵ near the critical value. The field value was measured 300 units of time after the intersection of the initial trajectories, that is $300 + x_0/v_i$ units of time after the start of the simulation. The black rectangle to the right indicates the near-critical region plotted in figure 21.

	ϵ	ω_1	ω_2	ω_3	ω_4	ω_5
Maxima:						
	0.131	0.9951				
	2.171	0.4931	0.8606	0.9927		
	2.597	0.0906	0.6284	0.7679	0.9057	0.9978
Minima:						
	1.471	0.7522	0.9796			
	2.444	0.3132	0.7565	0.9305		
	2.601	0.0755	0.6200	0.7513	0.8868	0.9896

Table 2. Spectral structure at extreme points

that some higher nonlinear term (presumably fourth order) is responsible for the minima of the critical velocity.

5.2 Double kink collisions near the critical value of ϵ

For $\epsilon > 2$, a false vacuum appears at $\phi = \pi$ between the true vacua at $\phi = 0$ and $\phi = 2\pi$. The presence of this false vacuum deforms the kink, splitting it into two smaller subkinks, which become more and more separated as $\epsilon \rightarrow \epsilon_{cr}$, as illustrated in figure 2. The eigenvalue of the first internal mode ω_1 rapidly approaches zero as this mode smoothly transforms

into an antisymmetric linear combination of the translational modes of the subkinks, as explained in section 2.4. Similarly, a symmetric combination of these modes corresponds to the translational mode ω_0 .

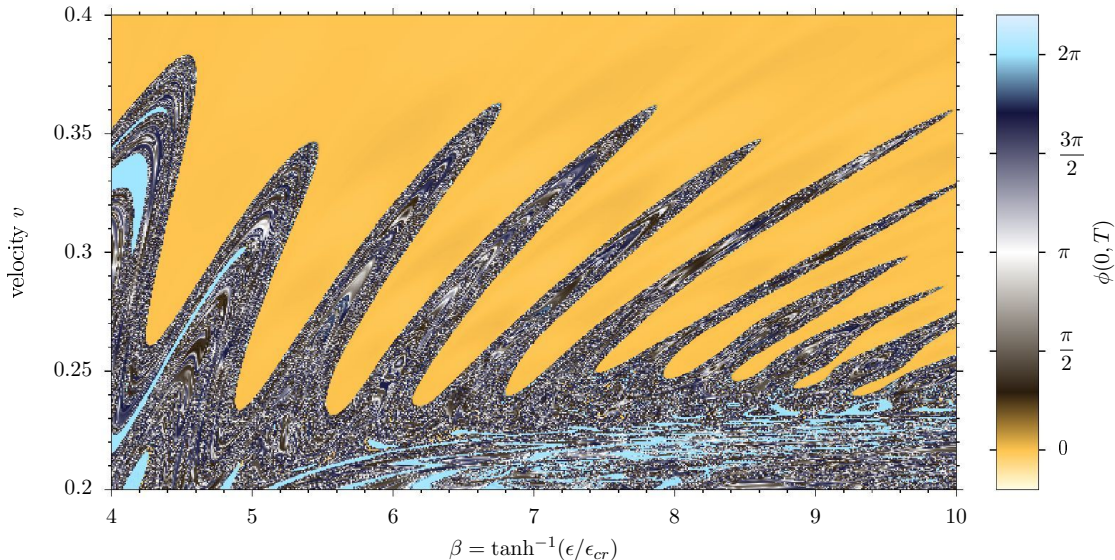


Figure 21. The near-critical region of figure 20. The range $4 \dots 10$ of the horizontal parameter $\beta = \tanh^{-1}(\epsilon/\epsilon_{cr})$ corresponds to ϵ running from 2.608195 to 2.609946. For these near-critical values of ϵ the antikink and kink have increased widths, and so for this plot they were placed further apart at $t = 0$, at $x = -40$ and $x = 40$. The dangers of placing the initial kinks and antikinks too close together can be seen by examining figure 29 below.

The oscillations of the critical velocity become more extreme as ϵ_{cr} is approached, their ‘waves’ ultimately overhanging in a series of spines as ϵ approaches ϵ_{cr} , as seen in figure 21, where for better resolution we used $\beta = \tanh^{-1}(\epsilon/\epsilon_{cr})$ instead of ϵ for the horizontal scale. In preparing this figure we measured the central field, as for our other scans, at a time $T = 300$ after the initial collision. Especially for larger values of β , the final value of the field at the origin may not have settled down by this time, and so we made some lower-resolution scans with longer evolution times. These showed that the yellow spaces between the bases of the spines have a tendency to close with time, but the further away from the base, or the smaller the value of β , the closer the spines shown in figure 21 were to their asymptotic forms. The white-grey-black regions of these spines indicate points where the incident $\bar{K}K$ pair annihilate to a centrally-located bion. Within the spines there are also (yellow) windows and (light blue) pseudowindows forming meandering stripes, where instead of the centrally located bion either a $\bar{K}K$ pair or a pair of escaping bions is produced. A cross-section of the right-hand edge of one of these spines, exhibiting both windows and pseudowindows, is shown in figure 22.

This surprisingly intricate structure appears to be associated with the dissociation of the kinks into pairs of subkinks in this regime. Related issues were recently discussed

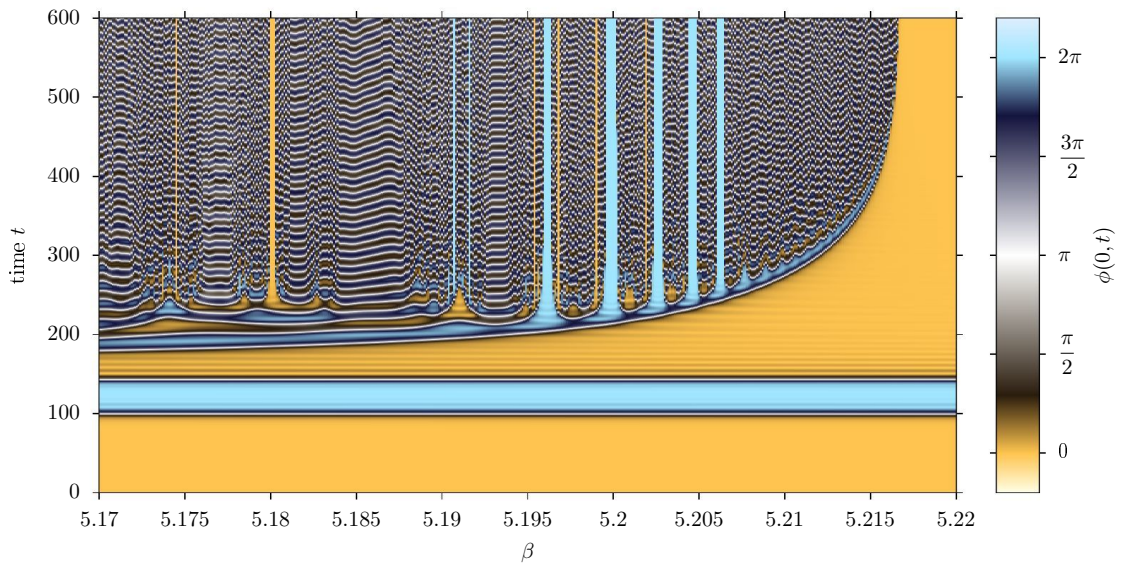


Figure 22. Field at $x = 0$ for initial velocity $v = 0.3$ and a range of β cutting into the right-hand edge of the second ‘porcupine spine’ in figure 21, showing both windows and pseudowindows.

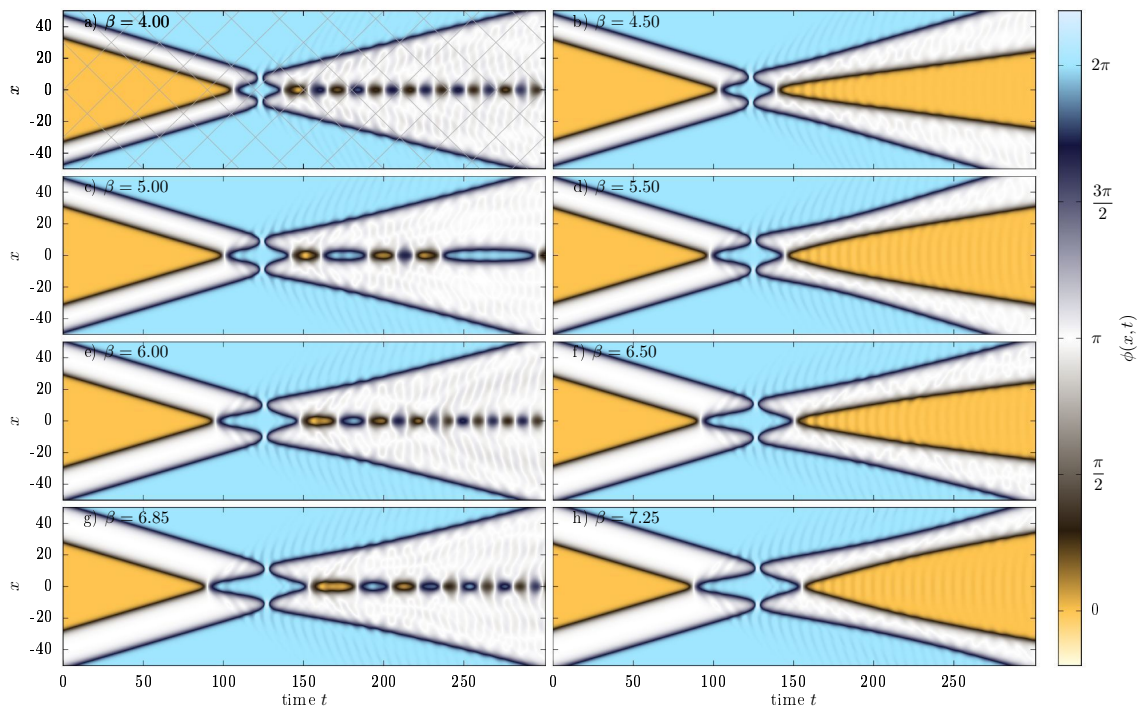


Figure 23. Example collisions with initial velocity $v = 0.3$ for a variety of values of β , showing the decomposition of the initial collision into four subkink collisions.

in [36], but in our model we can tune the distance between the half-kinks by varying the deformation parameter ϵ , and make the double kinks infinitely wide as $\epsilon \rightarrow \epsilon_{cr}$. The initial $\bar{K}K$ collision no longer happens as a single event, but rather splits into four subcollisions

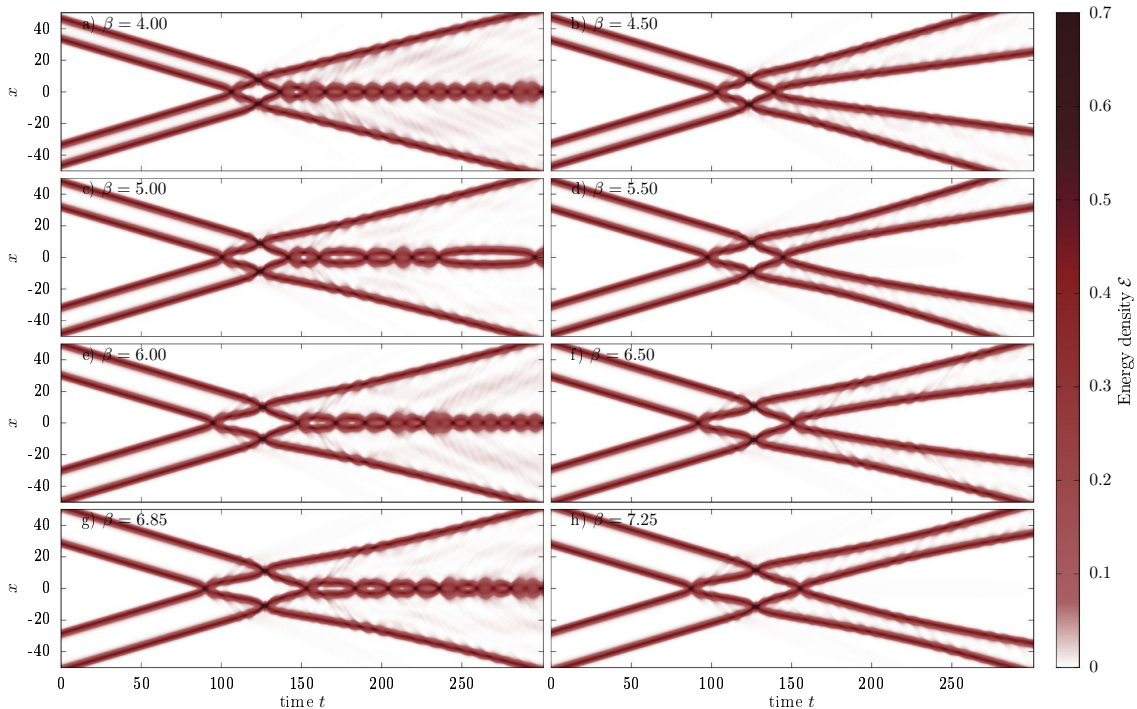


Figure 24. Energy density plots for the collisions shown in figure 23.

between the weakly bound constituent subkinks, with the fourth collision being key in determining the ultimate fate of the process. Some examples are shown in figure 23, while figure 24 shows the corresponding energy densities, highlighting the fragmented nature of the kinks in this regime. The first of the four subcollisions results in a bounce of the inner subkinks combined with a vacuum flip at the centre. The inner subkinks, moving slightly slower than before, then collide with the outer subkinks which arrive slightly later due to the extended structure of the full defect, and bounce back again. At least for the processes shown in figure 26, these returning subkinks are moving faster than were the outgoing subkinks that resulted from the first bounce. This might be surprising, but note that the outer subkinks arrive at the second subcollision travelling at full speed, while the outgoing inner subkinks are moving more slowly, so the rest frame for the second subcollision is moving towards the centre. From this point the scenarios differ depending on the velocity and β . The ingoing subkinks can annihilate at the centre to form a bion surrounded by a region of false vacuum, as in the processes plotted in the left-hand columns of figures 23 and 24. These processes correspond to points inside the first four spines shown in figure 21. Alternatively, the inner subkinks can escape from this fourth subcollision to pair off again with the outer subkinks, as in the processes shown in the right-hand columns of figures 23 and 24, with the vacuum at the centre flipping back to its original value. These correspond to points in the yellow-coloured regions between the spines.

This subkink capture/escape scenario is itself subject to a resonance mechanism, signs

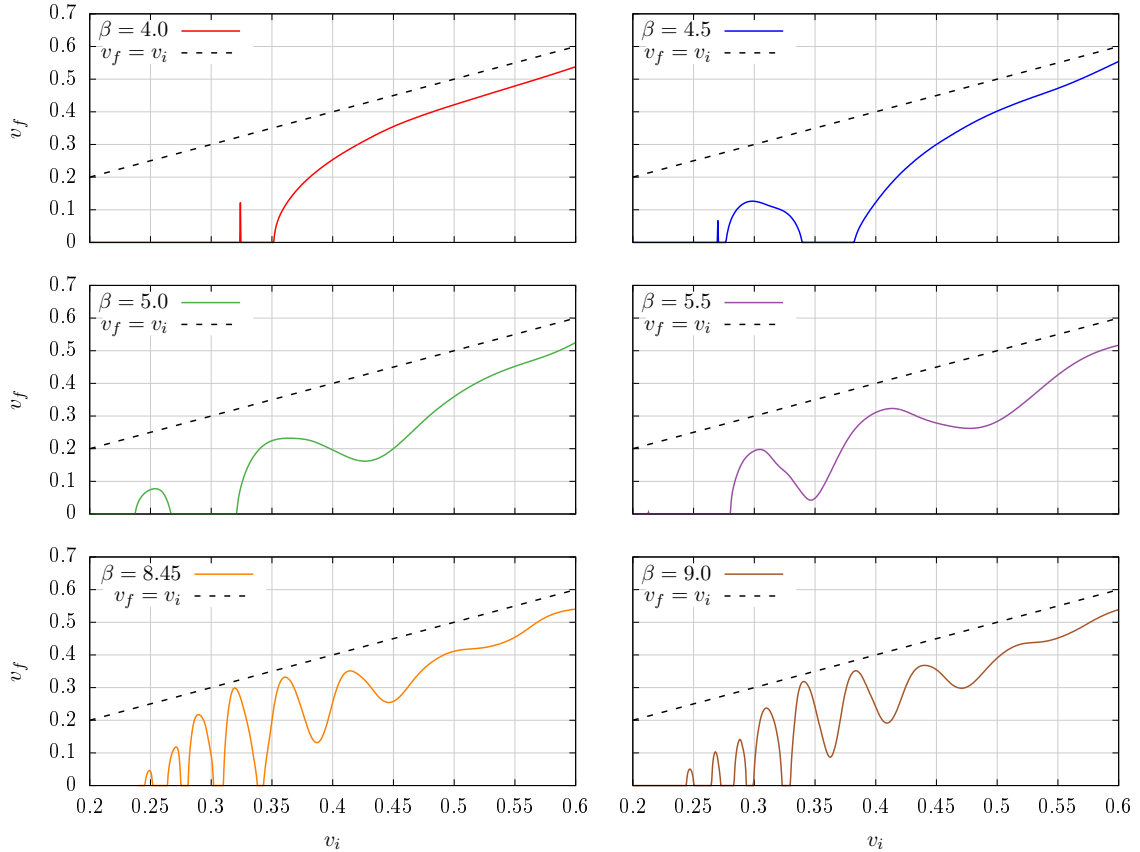


Figure 25. Inner subkink velocity shortly after the second subkink – subkink collision at $x = 0$ as a function of initial velocity in the near-critical region, illustrating the mechanism for the formation of the overhanging windows.

of which can be seen by counting the oscillations in the false vacuum visible between the first and second subcollisions in the processes shown in the right-hand column of figure 23. Figure 25 illustrates aspects of this scenario in more detail. The final velocity of the inner kink after the second central subcollision reveals some oscillational dependence on the initial velocity. This is very different from the monotonic growth above the upper critical velocity observed in the case of collisions of unexcited defects. However, exactly this feature was recently observed in [29] in the case of scattering of wobbling kinks. In that paper it was shown that if the excitation of the kinks is large enough it can lead to the appearance of new windows above the upper critical velocity. This is exactly the same effect that we observe for larger values of β with the exception that the excitation is not bound to the subkinks but is a superposition of radiation and inner oscillations of the double kink. Scanning through figure 25 as β varies gives a good intuition of how the spines in figure 21 are formed.

More complicated evolutions after the fourth subcollision are also possible, leading to the appearance of windows and pseudowindows within the spines, provided suitable

resonance conditions are met. Figure 26 shows three examples corresponding to three of the pseudowindows visible in figure 22, and one more showing the field evolution just outside the spine shown in that figure.

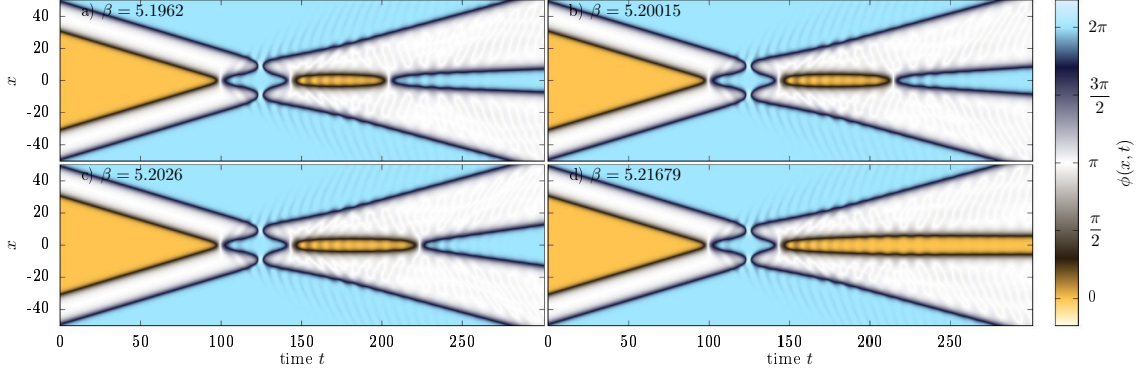


Figure 26. Example collisions with initial velocity $v = 0.3$ for a variety of values of β . In the first three cases a subsequent resonant collision leads to the formation of a pseudowindow.

The presence of the outer subkinks can also disturb the long-term evolution of the system. When a central bion is formed, the outer subkinks initially escape from the centre of collision, but because of the presence of the false vacuum they will always return and recollide with the bion at the centre. The time scale for this recollision is large, comparable with the period of the lowest oscillations of the double kink, which is of order e^β (see section 2.4). The collision between the returning outer subkinks and the bion is a chaotic process depending on many factors including the velocity of the incoming subkinks, the amplitude and the phase of the bion at the moment of the collision, and omnipresent radiation.

Some examples of such collisions are shown in figure 27. One striking feature is that near ϵ_{cr} large bubbles of the false vacuum can be created (white regions). Such bubbles tend to shrink but the presence of the central bion can impede their vanishing, as in plots (d), (f) and (i) of figure 27. In many cases as a final result two bions are ejected from the collision centre (plots (a), (b), (c) and (h) of figure 27). These events lie in the pseudowindows introduced above, signalled by regions of light blue colour on figures 17 and 20.

Figure 28 shows a further example. After the initial collision a false vacuum bubble with an unstable lump (described in section 2.5) at centre is created. The field profile matches the profile of the lump out to $x \approx \pm 15$, beyond which the outer subkinks connect with the true vacuum, as shown in figure 28 (b). At $t \approx 160$ the unstable lump decays, two subkinks being ejected only to bounce off the outer subkinks and recollide at centre, forming a bion. This bion survives the first collision with the outer subkinks around $t \approx 350$. Its profile is encapsulated in the profile of the unstable lump (figure 28 (c)). In a sense the lump can be thought of as a critical profile of a bion with zero frequency. During the second collision at $t \approx 640$ the bion is highly perturbed and much of its energy is transferred to the outer subkinks, which clearly move with higher velocity after the bounce.

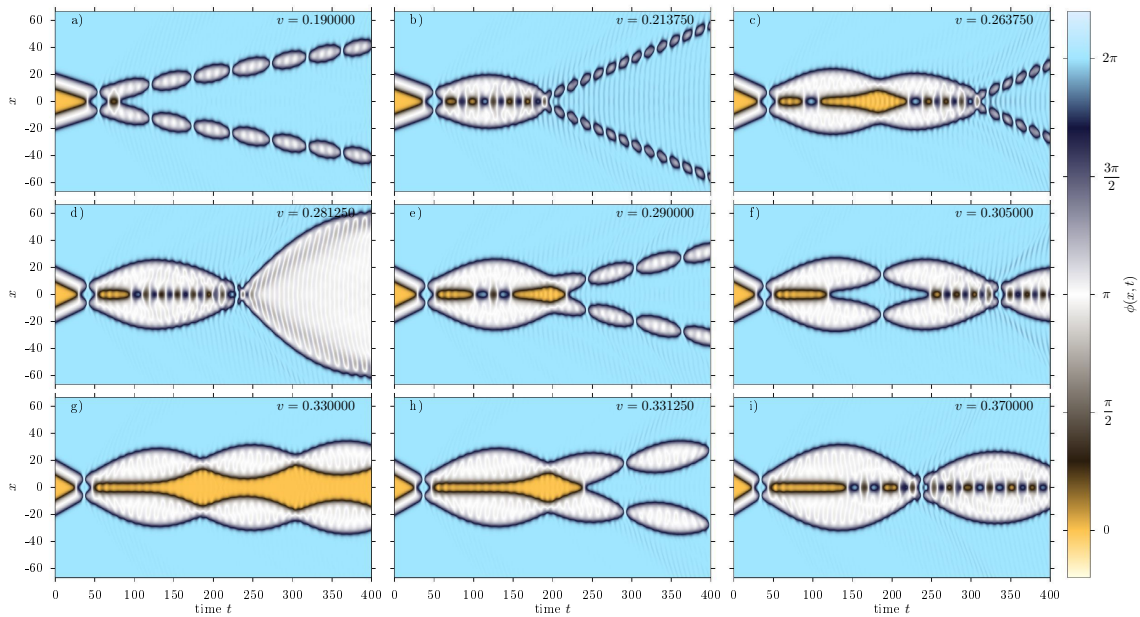


Figure 27. Example scattering processes for a variety of initial velocities at $\epsilon = 2.59935$ ($\beta = 3.09887$), illustrating the variety of behaviours of the subkinks after the initial four-way collision.

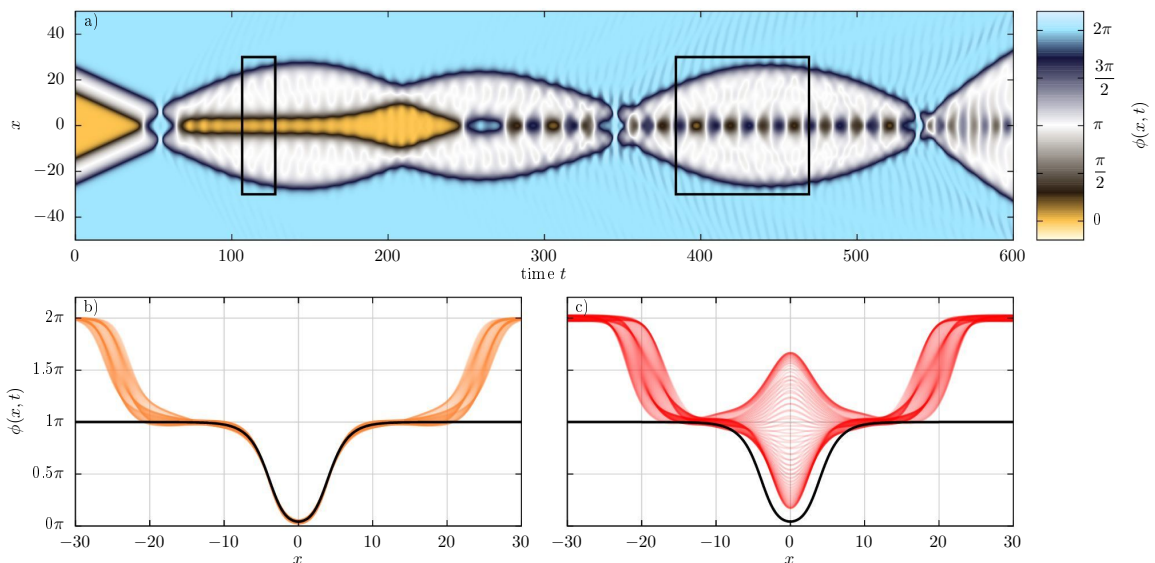


Figure 28. A further collision process, comparing the profiles of an intermediate state (b) and a bion (c) to the unstable lump solution (black line), for $\epsilon = 2.59935$ ($\beta = 3.09887$) and $v = 0.31$.

For ϵ very close to ϵ_{cr} , the energy of the false vacuum is only very slightly lifted above that of the true vacuum, and the vacuum pressure (which acts to shrink the region of false vacuum) is small. This means that other effects such as radiation pressure can be equally important. In this regime of our model the vacua on either side of the defect have significantly different masses associated with their small fluctuations, with the larger mass

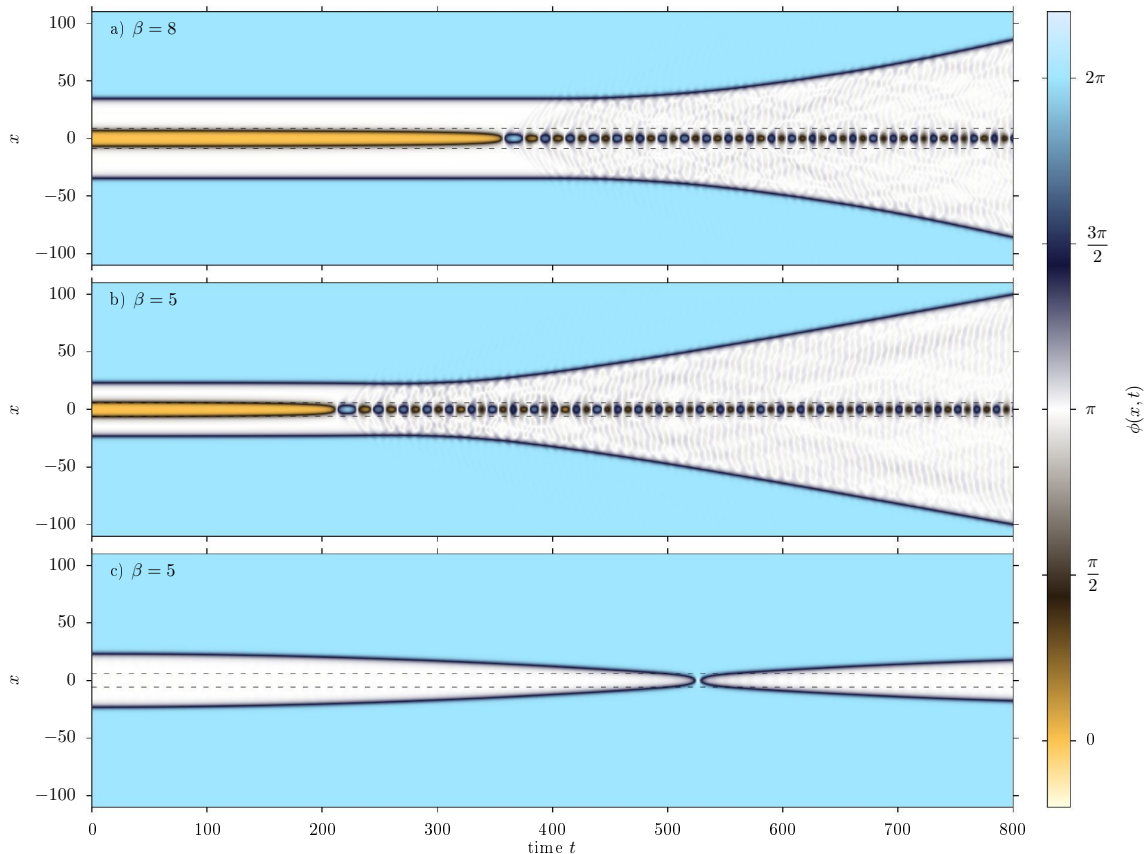


Figure 29. “Blowing bubbles”: two static kinks placed close to each other, for two values of ϵ near to ϵ_{cr} . The innermost subkinks attract each other and annihilate to create a bion, the radiation from which pushes the outer subkinks apart, thereby expanding the region of false vacuum. The final plot depicts the field evolution for the second case with the innermost subkinks removed, showing the collapse (and rebound) of the false vacuum bubble in the absence of radiation pressure.

belonging to the true vacuum. As a result, radiation pressure on this defect acts in the opposite direction to vacuum pressure, expanding regions of false vacuum. (Similar radiation pressure effects, albeit in the absence of vacuum pressure, were previously discussed in [37].) Signs of this effect can be seen in the plots in the left-hand column of figure 23, and in figure 26, in the slight acceleration of the outermost subkinks after the initial four-way collision. To illustrate the phenomenon and its relevance more clearly, the first two plots of figure 29 show the time-evolution of an initially-static configuration corresponding to a very closely-placed kink and antikink pair. The innermost subkinks, one from the kink and one from the antikink, attract each other and annihilate to create a bion a finite time after the start of the simulation. This bion then acts as a source of radiation embedded in a bubble of false vacuum, causing it to expand. The final plot shows that in the absence of radiation, the bubble instead contracts.

5.3 Small kinks at critical ϵ

To finish, we discuss the situation when $\epsilon = \epsilon_{cr}$ and our model has three exactly-degenerate vacua $\{0, \pi, 2\pi\}$. The full kink ceases to exist as a static configuration, and is replaced by two small kinks, $(0, \pi)$ and $(\pi, 2\pi)$, which are independent topological solitons, along with the corresponding small antikinks. While the potential is not quite the same, the scattering of these small kinks and/or small antikinks is very similar to that of kinks and antikinks in the triply-degenerate ϕ^6 model.

Two small kinks repel each other and their scattering shows no resonant phenomena. Two types of collisions between a small kink and a small antikink are possible, depending on which vacuum sits between them. The mass of the small perturbations around the $\phi = \pi$ vacuum is lower than that around $\phi = 0$ and $\phi = 2\pi$. When a $(\pi, 0)$ antikink collides with a $(0, \pi)$ kink, a potential well for the spectrum of small fluctuations is generated, within which many modes can exist. The width of the well depends on the distance between the defects. In this alignment the collisions do show a resonant structure, of the sort first discovered for the ϕ^6 model in [18]. The resonant structure for this case is shown in figure 30 (a).

By contrast, the collision of a $(0, \pi)$ kink to the left and a $(\pi, 0)$ antikink to the right creates a potential bump between the defects where no bound modes can exist, and as a result collisions of this type show no resonant structure, as seen in figure 30 (b).

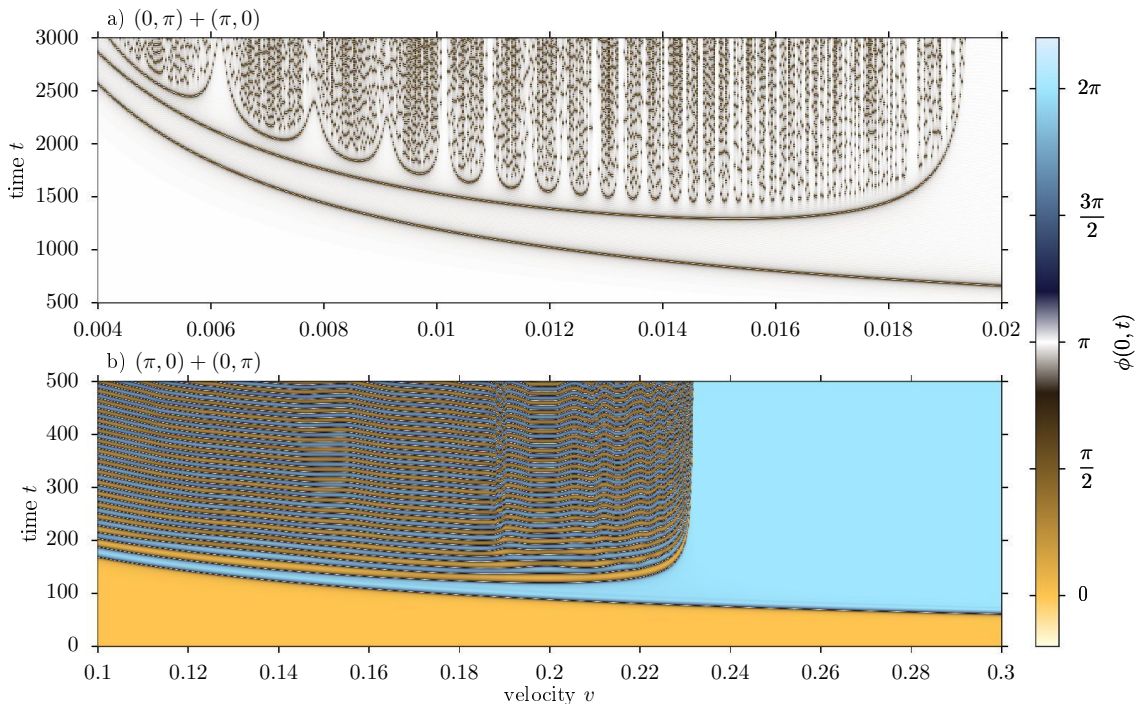


Figure 30. Collision of small antikinks and kinks for critical value $\epsilon = \epsilon_{cr}$ for alignments $(0, \pi) + (\pi, 0)$ (a) and $(\pi, 0) + (0, \pi)$ (b).

The pattern of true and false windows visible in figure 30 (a) is similar to that seen

previously, for the triply-degenerate ϕ^6 model, in [18]. However the colour scheme used in figure 30 – chosen for consistency with the one used elsewhere in this paper – makes the precise structure hard to discern.

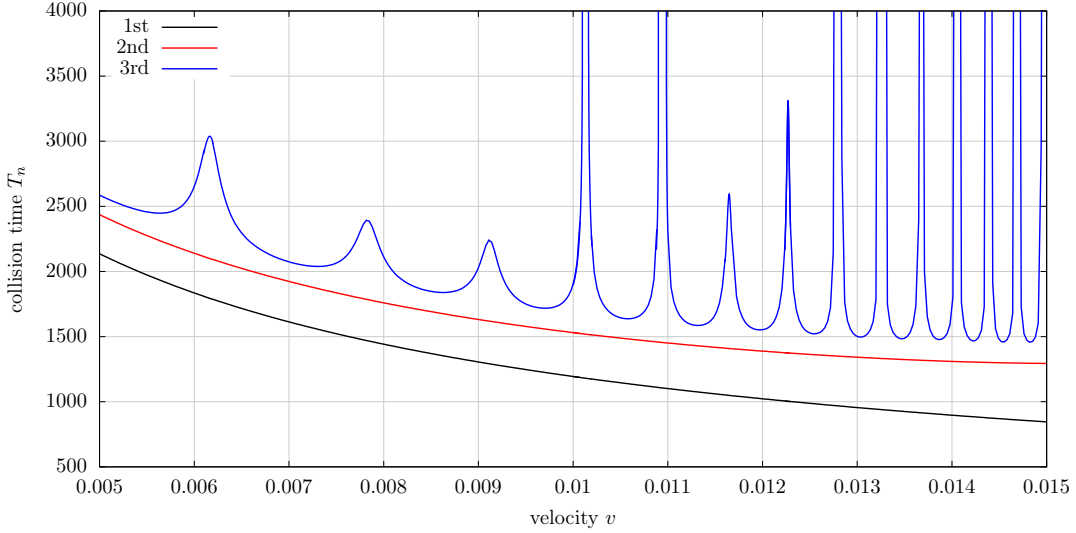


Figure 31. A closer look at the processes shown in figure 30 (a), showing the times to the first, second and third bounces for the scattering of small kinks and antikinks in the $(0, \pi) + (\pi, 0)$ configuration at $\epsilon = \epsilon_{cr}$.

Figure 31, which should be compared with figure 1 (e) of [18], shows a more detailed picture. Similar to the situation for the ϕ^6 model, but different from the sequences of closing windows seen earlier in this paper, we see that true and false windows are interleaved, something which might be associated with the fact that multiple resonant frequencies play a role in these cases. However the patterns are slightly different – for the ϕ^6 model there is a single isolated false window directly following the first true window, while here two true windows are followed by two false ones. An interesting challenge to any effective model of kink – antikink collisions in models of this type, where the resonant modes live in the gap between the colliding solitons, would be to reproduce this distinction.

6 Conclusions

In this paper we have studied the dynamical properties of a scalar field theory interpolating between the completely integrable sine-Gordon model, the usual ϕ^4 theory, and a ϕ^6 -like theory with three degenerate vacua. Our numerical simulations of the collisions between kinks and antikinks in the model revealed a rich diversity of behaviours and suggest a number of avenues for further investigation.

For $\epsilon \ll 1$ the key feature of the model is the breaking of integrability. We identified the role of the false vacuum in the smooth transition from the kink - antikink reflection

that occurs for $\epsilon > 0$ to the transmission found at $\epsilon = 0$. Associated with this is a sharp decrease in the critical velocity $v_{cr}(\epsilon)$, down to zero at $\epsilon = 0$ where integrability is restored. This is clear from our numerical results, but an analytic understanding of the behaviour of $v_c(\epsilon)$ for $\epsilon \ll 1$ would be very valuable. This regime would also be a good starting-point for an investigation of the quantum theory of this model.

In the neighbourhood of $\epsilon = 1$, we saw a smooth deformation of the ϕ^4 picture; again we would like to understand the dependence of $v_c(\epsilon)$ (and indeed the window locations) on ϵ from an analytic point of view. At both ends of this regime, resonance windows transition from true to false, starting with those at the lowest velocities. As things stand this is a numerical observation.

Beyond $\epsilon \approx 1.5$ the structure of the resonance windows becomes richer and more chaotic, with the emergence of novel structures that we called pseudowindows. In spite of the increased complexity of the behaviour of the model in this regime, we did see some signs of regularity, as reported in table 2.

The region $\epsilon \rightarrow \epsilon_{cr}$ is particularly intriguing. Our zoomed-in scans, figures 20 and 21, revealed a novel and unexpected structure of ‘spines’, which we associated with the emergence of an internal structure to our kinks in this limit. We identified some of the relevant mechanisms, in particular in the decomposition of individual kink - antikink collisions into four subcollisions, but more work is needed to pin down the details. Preliminary studies show that similar structures arise in the somewhat-simpler model studied by Christ and Lee in [25]. Numerical work in this regime is particularly delicate as the presence of the false vacuum means that some relevant processes take place over extremely long timescales, and whether greater regularity will emerge in the extreme limit $\epsilon \rightarrow \epsilon_{cr}$, $\beta \rightarrow \infty$ remains an open question; but these same effects make the model in this regime an excellent arena for the study of phenomena such as radiation pressure. In this region we also observed the formation of bions/oscillons submerged in a bubble of false vacuum. Their shapes were bounded by the profile of an unstable lump, a static solution consisting of two sub-kinks placed in unstable equilibrium, balancing false vacuum pressure against the mutual attraction between subkinks.

Finally, exactly at the limiting value $\epsilon = \epsilon_{cr}$ a triply-degenerate vacuum structure similar to the ϕ^6 model was restored. The subkinks become fully independent defects and their collisions, characteristic of non-symmetric kinks, happen with very similar mechanisms to those found in the ϕ^6 model. In spite of these similarities, the structure of false and true windows was different.

To conclude, kink scattering in the deformed sine-Gordon model exhibits a remarkable variety of phenomena. Some of these we have analysed in detail, while others we have merely pointed out, and merit further study in their own right. We also expect that many of these newly found effects will be observed in other models, but we will leave the investigation of this question for future work.

Acknowledgments

YS gratefully acknowledges partial support of the Ministry of Education of Russian Federation, project FEWF-2020-0003. TR wishes to thank National Science Centre, grant number 2019/35/B/ST2/00059. PED is grateful for support from the European Union’s Horizon 2020 research and innovation programme under the Marie Skłodowska-Curie grant agreement No. 764850, SAGEX, and from the STFC under consolidated grant ST/T000708/1 “Particles, Fields and Spacetime”.

References

- [1] N. S. Manton and P. M. Sutcliffe, *Topological solitons*. Cambridge monographs on mathematical physics. Cambridge University Press, Cambridge, July, 2004.
- [2] T. Vachaspati, *Kinks and Domain Walls: An Introduction to Classical and Quantum Solitons*. Cambridge University Press, 2006.
- [3] Y. M. Shnir, *Topological and Non-Topological Solitons in Scalar Field Theories*. Cambridge University Press, 7, 2018.
- [4] O. Babelon, D. Bernard and M. Talon, *Introduction to Classical Integrable Systems*. Cambridge Monographs on Mathematical Physics. Cambridge University Press, 2003, [10.1017/CBO9780511535024](https://doi.org/10.1017/CBO9780511535024).
- [5] L. Ferreira, G. Luchini and W. J. Zakrzewski, *The concept of quasi-integrability for modified non-linear Schrodinger models*, *JHEP* **09** (2012) 103, [[1206.5808](https://arxiv.org/abs/1206.5808)].
- [6] L. Ferreira and W. J. Zakrzewski, *The concept of quasi-integrability: a concrete example*, *JHEP* **05** (2011) 130, [[1011.2176](https://arxiv.org/abs/1011.2176)].
- [7] D. Ullmo, M. Grinberg and S. Tomsovic, *Near-integrable systems: Resonances and semiclassical trace formulas*, *Phys. Rev. E* **54** (Jul, 1996) 136–152.
- [8] M. Remoissenet and M. Peyrard, *A new simple model of a kink bearing hamiltonian*, *Journal of Physics C: Solid State Physics* **14** (jun, 1981) L481–L485.
- [9] M. Peyrard and D. Campbell, *Kink antikink interactions in a modified sine-Gordon Model*, *Physica D* **9** (1983) 33–51.
- [10] B. A. Malomed, *Inelastic interactions of solitons in nearly integrable systems. ii*, *Physica D: Nonlinear Phenomena* **15** (1985) 385 – 401.
- [11] F. Zhang, Y. S. Kivshar, B. A. Malomed and L. Vázquez, *Kink capture by a local impurity in the sine-gordon model*, *Physics Letters A* **159** (1991) 318 – 322.
- [12] R. Arthur, P. Dorey and R. Parini, *Breaking integrability at the boundary: the sine-Gordon model with Robin boundary conditions*, *J. Phys. A* **49** (2016) 165205, [[1509.08448](https://arxiv.org/abs/1509.08448)].
- [13] P. Anninos, S. Oliveira and R. Matzner, *Fractal structure in the scalar lambda $(\phi^{**2-1})^{**2}$ theory*, *Phys. Rev. D* **44** (1991) 1147–1160.
- [14] D. K. Campbell, J. F. Schonfeld and C. A. Wingate, *Resonance Structure in Kink - Antikink Interactions in ϕ^4 Theory*, *Physica D* **9** (1983) 1.

- [15] R. H. Goodman and R. Haberman, *Kink-antikink collisions in the ϕ^4 equation: The n -bounce resonance and the separatrix map*, *SIAM J. Applied Dynamical Systems* **4** (2005) 1195–1228.
- [16] V. Makhankov, *Dynamics of Classical Solitons In Nonintegrable Systems*, *Phys. Rept.* **35** (1978) 1–128.
- [17] M. Moshir, *Soliton - Anti-soliton Scattering and Capture in $\lambda\phi^4$ Theory*, *Nucl. Phys. B* **185** (1981) 318–332.
- [18] P. Dorey, K. Mersh, T. Romanczukiewicz and Y. Shnir, *Kink-antikink collisions in the ϕ^6 model*, *Phys. Rev. Lett.* **107** (2011) 091602, [[1101.5951](#)].
- [19] I. Takyi and H. Weigel, *Collective Coordinates in One-Dimensional Soliton Models Revisited*, *Phys. Rev. D* **94** (2016) 085008, [[1609.06833](#)].
- [20] H. Weigel, *Kink-Antikink Scattering in φ^4 and ϕ^6 Models*, *J. Phys. Conf. Ser.* **482** (2014) 012045, [[1309.6607](#)].
- [21] H. Weigel, *Collective Coordinate Methods and Their Applicability to φ^4 Models*, [1809.03772](#).
- [22] C. Adam, T. Romanczukiewicz and A. Wereszczynski, *The ϕ^4 model with the BPS preserving defect*, *JHEP* **03** (2019) 131, [[1812.04007](#)].
- [23] N. S. Manton, K. Oleś, T. Romańczukiewicz and A. Wereszczyński, *Kink moduli spaces: Collective coordinates reconsidered*, *Phys. Rev. D* **103** (2021) 025024, [[2008.01026](#)].
- [24] N. S. Manton, K. Oles, T. Romanczukiewicz and A. Wereszczynski, *Collective coordinate model of kink-antikink collisions in ϕ^4 theory*, [2106.05153](#).
- [25] N. H. Christ and T. D. Lee, *Quantum expansion of soliton solutions*, *Phys. Rev. D* **12** (Sep, 1975) 1606–1627.
- [26] F. C. Simas, A. R. Gomes, K. Z. Nobrega and J. C. R. E. Oliveira, *Suppression of two-bounce windows in kink-antikink collisions*, *JHEP* **09** (2016) 104, [[1605.05344](#)].
- [27] A. Demirkaya, R. Decker, P. G. Kevrekidis, I. C. Christov and A. Saxena, *Kink dynamics in a parametric ϕ^6 system: a model with controllably many internal modes*, *JHEP* **12** (2017) 071, [[1706.01193](#)].
- [28] P. Dorey, T. Romanczukiewicz and Y. Shnir, *Staccato radiation from the decay of large amplitude oscillons*, *Phys. Lett. B* **806** (2020) 135497, [[1910.04128](#)].
- [29] A. Alonso Izquierdo, J. Queiroga-Nunes and L. M. Nieto, *Scattering between wobbling kinks*, *Phys. Rev. D* **103** (Feb, 2021) 045003.
- [30] J. Ashcroft, M. Eto, M. Haberichter, M. Nitta and M. Paranjape, *Head butting sheep: Kink Collisions in the Presence of False Vacua*, *J. Phys. A* **49** (2016) 365203, [[1604.08413](#)].
- [31] A. R. Gomes, F. Simas, K. Nobrega and P. Avelino, *False vacuum decay in kink scattering*, *JHEP* **10** (2018) 192, [[1805.00991](#)].
- [32] I. Kobzarev, L. Okun and M. Voloshin, *Bubbles in Metastable Vacuum*, *Sov. J. Nucl. Phys.* **20** (1975) 644–646.
- [33] S. R. Coleman, *The Fate of the False Vacuum. 1. Semiclassical Theory*, *Phys. Rev. D* **15** (1977) 2929–2936.

- [34] M. Voloshin, *Decay of false vacuum in (1+1)-Dimensions*, *Yad. Fiz.* **42** (1985) 1017–1026.
- [35] V. Kiselev and Y. Shnir, *Forced topological nontrivial field configurations*, *Phys. Rev. D* **57** (1998) 5174–5183, [[hep-th/9801001](#)].
- [36] Y. Zhong, X.-L. Du, Z.-C. Jiang, Y.-X. Liu and Y.-Q. Wang, *Collision of two kinks with inner structure*, *JHEP* **02** (2020) 153, [[1906.02920](#)].
- [37] T. Romańczukiewicz, *Could the primordial radiation be responsible for vanishing of topological defects?*, *Phys. Lett. B* **773** (2017) 295–299, [[1706.05192](#)].